DRAFT VERSION AUGUST 14, 2026
Typeset using LaTeX **twocolumn** style in AASTeX631

The JWST Proto-PAH project: Infrared spectroscopy of highly evolved carbon-rich objects

G. C. SLOAN,[1,2] KEVIN VOLK,[1] J. CAMI,[3,4] DEBAYAN DAS,[3] C. BHATT,[3,4] NICHOLAS CLARK,[3,4] KATHLEEN E. KRAEMER,[5] B. ARINGER,[6,7] J. BERNARD-SALAS,[8,9] HARRIET L. DINERSTEIN,[10] D. A. GARCÍA-HERNÁNDEZ,[11,12] M. A. GÓMEZ-MUÑOZ,[13,14,15] JIALU LI,[11,12] A. MANCHADO,[11,12,16] MIKAKO MATSUURA,[17] ELS PEETERS,[3,4] A. RICCA,[18,19] R. SAHAI,[20] N. C. STERLING,[21] G. M. WAHLGREN,[1] AND A. A. ZIJLSTRA[22]

[1]*Space Telescope Science Institute, 3700 San Martin Drive, Baltimore, MD 21218, USA*
[2]*Department of Physics and Astronomy, University of North Carolina, Chapel Hill, NC 27599-3255, USA*
[3]*Department of Physics and Astronomy, The University of Western Ontario, London, ON N6A 3K7, Canada*
[4]*Institute for Earth and Space Exploration, The University of Western Ontario, London, ON N6A 3K7, Canada*
[5]*Institute for Scientific Research, Boston College, 140 Commonwealth Avenue, Chestnut Hill, MA 02467, USA*
[6]*Theoretical Astrophysics, Department of Physics and Astronomy, Uppsala University, Box 516, 751 20 Uppsala, Sweden*
[7]*Department of Astrophysics, University of Vienna, Türkenschanzstraße 17, 1180 Wien, Austria*
[8]*ACRI-ST, Centre dEtudes et de Recherche de Grasse (CERGA), 10 Av. Nicolas Copernic, 06130 Grasse, France*
[9]*INCLASS Common Laboratory, 10 Av. Nicolas Copernic, 06130 Grasse, France*
[10]*Department of Astronomy, University of Texas at Austin, Austin, TX 78712, USA*
[11]*Instituto de Astrofísica de Canarias, C/ Via Láctea s/n, E-38205 La Laguna, Spain*
[12]*Departamento de Astrofísica, Universidad de La Laguna (ULL), E-38206 La Laguna, Spain*
[13]*Departament de Física Quàntica i Astrofísica (FQA), Universitat de Barcelona (UB),c. Martí i Franquès, 1, 08028 Barcelona, Spain*
[14]*Institut de Ciències del Cosmos (ICCUB), Universitat de Barcelona (UB), c. Martí i Franquès, 1, 08028 Barcelona, Spain*
[15]*Institut d'Estudis Espacials de Catalunya (IEEC), Edifici RDIT, Campus UPC, 08860 Castelldefels (Barcelona), Spain*
[16]*Consejo Superior de Investigaciones Científicas (CSIC), Spain*
[17]*Cardiff Hub for AstrophysicsResearch and Technology(CHART), PACES, Cardiff University, The Parade,Cardiff CF24 3AA, UK*
[18]*NASA Ames Research Center, MS 245-6, Moffett Field, CA 94035-1000, USA*
[19]*Carl Sagan Center, SETI Institute, 339 Bernardo Avenue, Suite 200, Mountain View, CA 94043, USA*
[20]*Jet Propulsion Laboratory, MS 183-900, 4800 Oak Grove Dr., California Institute of Technology, Pasadena, CA 91109, USA*
[21]*University of West Georgia, Carrollton, GA 30118, USA*
[22]*Jodrell Bank Centre for Astrophysics, The University of Manchester, Manchester, M13 9PL, UK*

ABSTRACT

Spectra from JWST reveal the rich chemistry of gas and dust around seven carbon-rich objects in the Magellanic Clouds as they evolve from the asymptotic giant branch (AGB) to planetary nebulae. As the hot central star is increasingly exposed, polycyclic aromatic hydrocarbons (PAHs) replace the amorphous carbon dust. The JWST spectra reveal strong emission and absorption at 3.4–3.5, 6.9, and 7.3 μm from aliphatic hydrocarbons bonded to aromatic skeletons. The spectra show emission and absorption bands from many gas-phase molecules, including H_2, CO, CN, CH_3, CH_4, C_2H_2, C_4H_2, C_6H_2, C_2H_4, C_6H_6, HCN, and HC_3N. Atomic lines include hydrogen in emission and absorption and forbidden lines in emission. Several molecules can exhibit P Cygni profiles from molecular outflows, including CO centered at 4.7 μm, C_4H_2 at 15.94 μm and C_6H_2 at 16.11 μm. This wealth of chemical clues adds to the information needed to understand how PAHs and related carbonaceous material form in the outflows of stars evolving away from the AGB.

Keywords: Extreme carbon stars (512) — Planetary nebulae (1249) — Circumstellar gas (241) — Circumstellar dust (236) — Polycyclic aromatic hydrocarbons (1280) — Infrared spectroscopy (2295)

1. INTRODUCTION

Carbon-rich post-asymptotic giant-branch (post-AGB) objects are rapidly evolving into planetary nebulae (PNe). As the mass loss exposes the core of the star, its effective temperature climbs from ∼3000 K to tens of thousands of degrees and the radiation field grows increasingly harsh. While

gcsloan@stsci.edu

amorphous carbon produces most of the dust emission from carbon stars on the AGB (Martin & Rogers 1987), polycyclic aromatic hydrocarbons (PAHs) and related species dominate in carbon-rich PNe (e.g., Gillett et al. 1973; Leger & Puget 1984; Allamandola et al. 1985). Once PAHs enter the interstellar medium, they can dominate the mid-infrared (MIR) emission from star-forming galaxies (e.g., Gillett et al. 1975; Willner et al. 1977; Brandl et al. 2006; Teplitz et al. 2007). PAHs may represent up to 15% of the total interstellar carbon budget (Snow & Witt 1995; Cesarsky et al. 2000). How they and related hydrocarbons form and develop are fundamental questions in astrophysics.

The PAH-like emission from carbon-rich post-AGB objects can look quite different from that of carbon-rich PNe. In the near-IR (NIR), a broad emission feature at 3.29 μm from C–H stretching in aromatic hydrocarbons is usually prominent in PNe. Post-AGB objects, though, can show stronger features at 3.4–3.5 μm (e.g., Geballe & van der Veen 1990; Geballe et al. 1992) arising from aliphatic C–H stretching modes (e.g., Bernstein et al. 1996; Joblin et al. 1996; Sandford et al. 2013). This mixture of aliphatic and aromatic hydrocarbons revealed in the NIR differs both from the amorphous carbon that came before on the AGB and the predominantly aromatic hydrocarbons that follow in PNe.

In the MIR, Peeters et al. (2002) classified PAH spectra based on the 6–9 μm spectral region of the Short-Wavelength Spectrometer (SWS; de Graauw et al. 1996) on the Infrared Space Observatory (ISO; Kessler et al. 1996). This range includes C–C modes in PAHs at 6.2, 7.65, and 7.85 μm, and an in-plane C–H bending mode at 8.6 μm (Allamandola et al. 1989). PNe generally have Class B emission, where the 7.85 μm component outshines the 7.65 μm component, in contrast to Class A spectra seen in star-forming regions, where the 7.65 μm component dominates. In Class B spectra, the 6.2 μm feature has shifted measurably to the red. The two class C spectra in the SWS database, both from Galactic carbon-rich post-AGB objects, have further shifts to the red at 6.2 μm and show an 8.2 μm emission feature instead of the usual 7.65 and 7.85 μm components.

The Infrared Spectrograph (IRS; Houck et al. 2004) on the Spitzer Space Telescope (Werner et al. 2004) found more Class C sources and added new classes. Sloan et al. (2007) suggested that Class C features arise from a higher ratio of aliphatic to aromatic hydrocarbons in radiation fields less harsh than those that excite Class A and B PAHs. Laboratory measurements confirm that the 6.2 μm feature shifts to the red in more aliphatic hydrocarbon samples (Pino et al. 2008). Matsuura et al. (2014) discovered unusual emission profiles at 7–9 μm in carbon-rich post-AGB objects in the Large Magellanic Cloud (LMC). Their newly defined Class D spectra have an additional emission component that fills in the usual minimum between the 7.85 μm C–C mode and the 8.6 μm in-plane C–H bending mode. They also found that some Class D sources have unusual structure at 11–14 μm, where C–H out-of-plane bending modes emit. The Class D spectra also show a broadened 6.2 μm emission feature. Sloan et al. (2014) divided the new class into D1 for relatively normal 11–14 μm spectral structure and D2 for spectra showing the 11.2 μm bending mode but with features at 12.3 and 13.3 μm instead of 12.0 and 12.7 μm. In short, these carbon-rich objects between the AGB and PNe possess a dust compoment with PAH-like characteristics, but decidedly different. We describe call carbonaceous material "proto-PAHs."

Carbon-rich post-AGB objects often also show a strong broad emission feature known as the 21 μm feature and discovered in spectra from the Infrared Astronomical Satellite (IRAS) mission (Kwok et al. 1989; Hrivnak & Kwok 1991). The sample of known 21 μm sources now numbers at least 31 (Volk et al. 2020), including nine in the Large and Small Magellanic Clouds (LMC and SMC; Matsuura et al. 2014; Sloan et al. 2014). Its carrier remains unidentified (Volk et al. 2020), but it usually appears in spectra that also show PAHs and related aliphatic material, suggesting that it arises in similar physical and chemical conditions (e.g., Kwok et al. 1989; Cerrigone et al. 2011).

The infrared spectra of carbon-rich post-AGB stars can show complex molecular hydrocarbon chemistries. Simple molecules such as acetylene (C_2H_2), C_3, and HCN are well-known absorbers in the envelopes of carbon stars (e.g., Hron et al. 1998; Aoki et al. 1998). The ISO spectrum of the Galactic post-AGB object AFGL 618 revealed absorption bands from larger hydrocarbons: diacetylene (C_4H_2), triacetylene (C_6H_2), and benzene (C_6H_6), as well as HC_3N and HC_5N (Cernicharo et al. 2001). Bernard-Salas et al. (2006) identified the same molecules (except HC_5N) in the Spitzer spectrum of the young Magellanic PN SMP LMC 011 and also identified ethylene (C_2H_4). Spitzer spectroscopy of MSX SMC 029 revealed Class C emission from PAHs and evidence for complex molecular absorption similar to SMP LMC 011, although only acetylene could be confirmed with the low-resolution spectra available (Kraemer et al. 2006).

To study the evolution of carbon-rich dust into PAHs during the critical post-AGB phase, we designed the JWST Proto-PAH Project to take advantage of the spectroscopic resolution, sensitivity, and wavelength coverage of the spectrometers on JWST (Gardner et al. 2023). The data from this program can address many questions raised by previous work. Do the previously seen broad and smooth features resolve into molecular band structure at higher resolution? What molecular bands can be detected at these resolutions? And what does this new information tell us about the evolution of carbon-rich dust from the AGB to PNe? A series of

papers beginning with this overview will address those questions.

This paper focuses on the nature of the sources in the sample and the identification of the dust features and molecular bands in the spectra. Section 2 describes the sample, the JWST observations, and the data reduction. Section 3 presents the JWST spectra and the feature identifications, and Section 4 provides light curves, spectral energy distributions (SEDs) and preliminary radiative-transfer models for the sources. Section 5 discusses the results, and Section 6 summarizes them.

2. SAMPLE AND SPECTRA

2.1. *Sample*

The JWST Cycle 3 program 4678 observed a sample of seven targets, all of them carbon-rich post-AGB objects in the LMC and the SMC. They were all previously observed by IRS on Spitzer. The sample includes two sources with Class D1 PAH spectra, two D2 sources, two sources known or suspected to have strong absorption spectra, and one Class B source to pair with SMP LMC 058, a PN with Class B PAH emission that was observed as a calibration target by JWST. Table 1 provides background information on these targets.

The absorption sources are SMP LMC 011 and MSX SMC 029. The LMC source does not show any PAH or PAH-like emission features (Bernard-Salas et al. 2006). The SMC source has suspected absorption bands along with Class C PAH emission (Kraemer et al. 2006). The remaining five sources in the newly observed sample were chosen because their IRS spectra had good signal-to-noise (S/N) ratios and were relatively free of artifacts and unusual features compared to other members of their class. That last condition means that they were not chosen randomly. These targets were originally observed in different Spitzer programs with different scientific goals and selection biases.

2.2. *Observations*

All seven targets in JWST program 4678 were observed in 2025 May and June in Cycle 3 in two spectroscopic modes, using NIRSpec (Jakobsen et al. 2022; Böker et al. 2023) and the Medium-Resolution Spectrometer (MRS; Argyriou et al. 2023) on the Mid-Infrared Instrument (MIRI; Wright et al. 2023). The observations were designed to achieve S/N $\geq$100 between 3.2 and 20 μm.

The NIRSpec observations were obtained with the fixed slit S200A1 (0.″2 width), the G395H grating, and the F290LP filter, which generated spectra at 2.88–3.68 and 3.79–5.12 μm. The gap in wavelength coverage results from the separation of the two NIRSpec detectors. The observations used a three-point dither pattern. The NIRSpec settings result in a spectral resolving power ($R \equiv \lambda/\Delta\lambda$) $\sim$ 2700.

The MRS observations used all three grating settings to obtain complete spectra from 4.9 to 28.7 μm. The observations used a 4-point dither pattern optimized for point sources, in the default negative direction, and optimized for "ALL MRS", which is equivalent to optimization for the shortest-wavelength channel. The MRS spectra have $R \sim$ 2000–3000 (see Pontoppidan et al. 2024, for details).

In addition to the data from program 4678, we include similar data for SMP LMC 058 from the JWST commissioning period and calibration for Cycle 1. The NIRSpec observations are from programs 1125 and 1492. Both use the same fixed slit and grating/filter configuration as program 4678. The observation from program 1125 used a three-point dither with three spectral dithers, for a total of nine exposures. For program 1492, the dither pattern used five cross-dispersion and three dispersion positions, for a total of 15 exposures. The MRS data used here were obtained in programs 1049 and 1523, but some had different dither patterns than for the other targets. These differences affect the calibration of the spectra, and for the MRS, the data reduction method.

2.3. *Reduction and calibration*

We reduced and calibrated the NIRSpec observations using the JWST Calibration Pipeline Version 2.0.0 (Bushouse, et al. 2026) with context version `jwst_1535.pmap`. We used the standard pipeline, except that we turned on two steps that are off by default. The `clean_flicker_noise` step was applied in both the `calwebb_detector1` and `calwebb_spec2` steps using default parameter values to remove correlated noise (Rauscher 2024). The `pixel_replace` step was applied in both the `calwebb_spec2` and `calwebb_spec3` stages with the default parameter values. This step estimates flux values for flagged detector pixels from neighbors in the two-dimensional spectral images.

For the MRS data, we used a development version of the pipeline (JWST 1.20.2dev) along with the point fixed-pattern correction (PFPC) developed specifically for point-sources by Gordon & Law (2026).[1] The PFPC extracts the spectra from the separate dither positions and calibrates them independently using similar observations of JWST standard stars. This method differs from the standard pipeline, which combines the dithers into a single data cube from which it extracts the spectrum. The PFPC removes residual fringing and residual flatfield errors from the data, provided that the science target is observed in the same positions on the MRS detectors as the calibration targets. This means that they must use the same dither pattern. A correction for residual fringing is

[1] https://github.com/STScI-MIRI/MRS-PFPC

Table 1. The Proto-PAH Sample

Target[a]	RA	Dec	Galaxy	PAH	JWST Observations				Date of Observation		
	J2000			Class	NIRSpec		MIRI/MRS		IRS	NIRSpec	MRS
	(degrees)				PID	Obs.	PID	Obs.	(MJD)	(MJD)	(MJD)
MSX SMC 029	9.193050	−73.526507	SMC	C/abs	4678	11	4678	1	53300	60825	60822
SMP LMC 011	72.907617	−67.088023	LMC	abs	4678	12	4678	2	53527	60825	60822
IRAS 05073−6752	76.807985	−67.812978	LMC	D1	4678	13	4678	3	54485	60825	60822
IRAS 06111−7023	92.633395	−70.411329	LMC	D1	4678	14	4678	4	54057	60825	60822
J004441[b]	11.171265	−73.360034	SMC	D2	4678	15	4678	5	54688	60831	60824
IRAS 05110−6616	77.794330	−66.214896	LMC	D2	4678	16	4678	6	54949	60825	60832
IRAS 05360−7121	83.857690	−71.332403	LMC	B	4678	17	4678	7	53992	60825	60831
SMP LMC 058	81.086445	−70.083778	LMC	B	1125	1	1049	1–2	53451	59746	59735
					1492	1	1523	3		59769	60074

[a] This paper uses shortened names for the IRAS and 2MASS sources.

[b] Full name: 2MASS J00444111−7321361.

built into the PFPC, because the phase offset and amplitude of the fringes as a function of wavelength depend on location on the detector (Gasman et al. 2025).

To remove discontinuities between the 12 spectral segments in each spectrum from the MRS, we used the regions of overlap to compute a scalar multiplicative correction for the entire segment, starting with Band 3A (11.6–13.5 μm) and propagating outward in both directions. These "stitching" corrections were generally less than 1%, except in some cases for Bands 1A, 4B, and 4C. We have not stitched the NIRSpec data.[2]

Because the MRS observations of SMP LMC 058 used a different dither pattern, we did not apply the PFPC. Instead, we used the standard pipeline output (JWST version 2.0.0, Build 12.3), with the residual-fringe correction. The final spectrum is a combination of three spectra, one taken during commissioning (PID 1049), and two taken a year later as part of the JWST Cycle 1 calibration (PID 1523). The stitching corrections for SMP LMC 058 were larger than for the program targets, but still within 1% between Bands 2C and 4B (10.0–24.5 μm).[3]

All of the spectra were calibrated primarily using observations of standard stars with models from the CALSPEC project (Gordon et al. 2022). The exception is the use of asteroids in the longest-wavelength segments of the MRS to interpolate at wavelengths directly affected by atomic absorption lines (Gordon & Law 2026) and to improve on the poor S/N of standard stars in Channel 4 (i.e., at wavelengths $>$ 18 μm; Law et al. 2025).

Figure 1 compares the JWST spectra from NIRSpec and the MIRI/MRS to the spectra from the IRS on Spitzer. JWST has given us the opportunity to obtain moderate-resolution spectra of the sample below 5 μm, providing our first look at the C–H stretching modes at 3.3–3.5 μm in these sources and molecular band structure from 2.85 to 5 μm. Past 5 μm, the MRS and IRS spectra show significant changes in the brightness of the two absorption sources in the 20 years between their observations. Section 4.1 confirms that those changes are real. Several other spectra show more subtle changes in brightness and spectral behavior.

3. JWST SPECTRAL RESULTS

The spectral results from the fixed slit in NIRSpec and the MIRI/MRS are too rich to fully investigate in a single paper. This section presents the initial spectroscopic identifications and leaves those results requiring modeling or rigorous analysis to more focused papers to follow.

Jones et al. (2023) investigated the MRS spectrum for SMP LMC 058. It displays broad, smooth dust features from SiC at $\sim$11.3 μm and Class B PAH emission, as Figure 1 shows. The spectrum also contains (at least) 50 emission lines, mainly hydrogen recombination lines or forbidden lines from metal ions. The spectrum from NIRSpec contains over 80 atomic emission lines, which complicates the analysis of the PAH features. We defer the analysis of SMP LMC 058 to future work (Sterling et al., in prep.). This

[2] The NIRSpec flux values fall below the MRS by an average of 9%, with a range of 7–15%, for the 7 targets in program 4678.

[3] The NIRSpec data are below the MRS by 21%, likely due to the small 0.″2 slit and slightly resolved nature of the target.

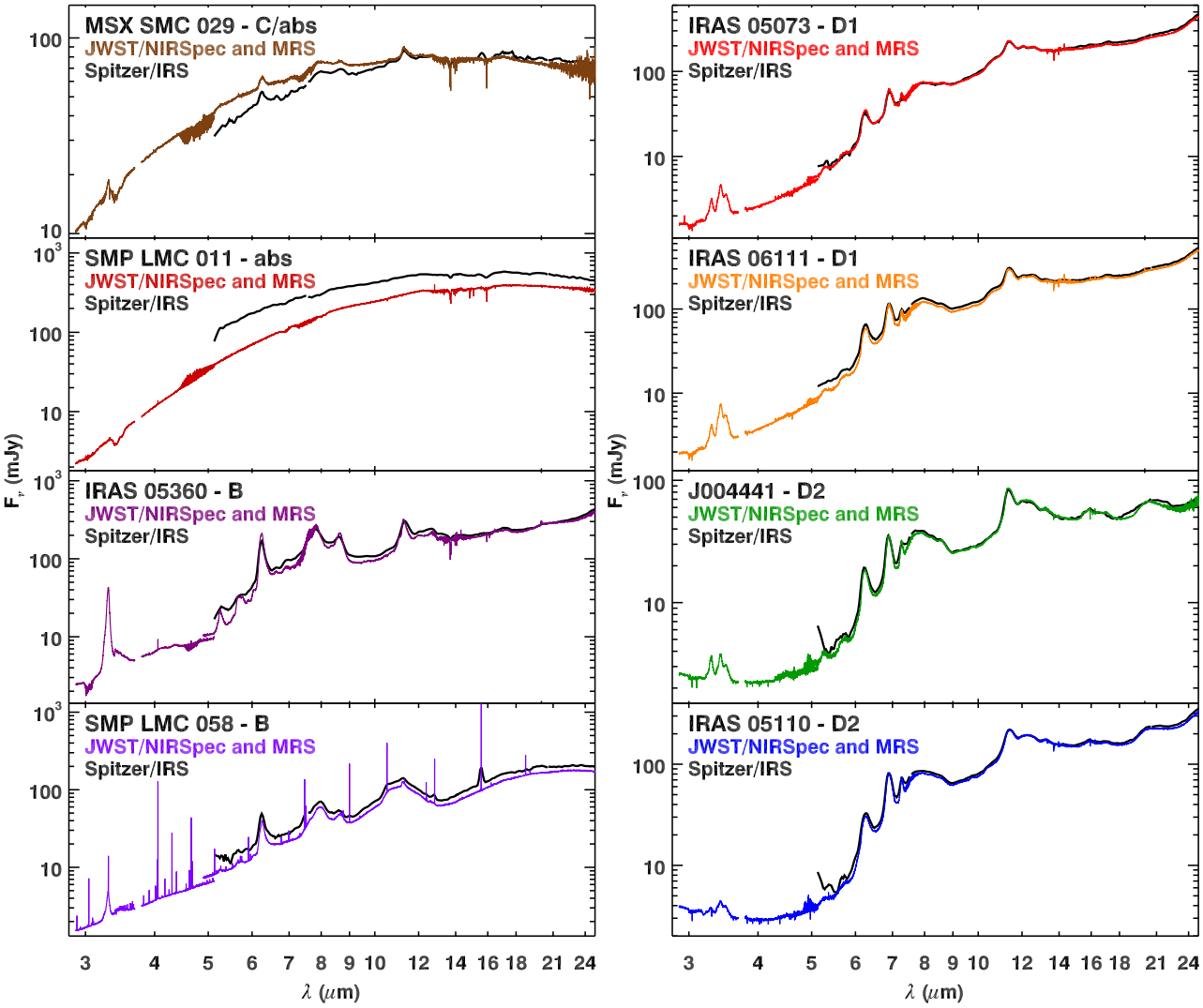

Figure 1. The NIRSpec and MIRI/MRS spectra of the seven sources in the Proto-PAH sample and SMP LMC 058, compared to the Spitzer/IRS spectra taken 16–20 years earlier. The calibration of the IRS spectra can be questionable near 5 μm, as the spectra of J004441 and IRAS 05110 show.

section will focus on the seven targets specifically part of the Proto-PAH program.

Table 2 summarizes the atomic and molecular contents of the spectra of the seven Proto-PAH sources. Sections 3.1 and 3.2 below describe the identifications in NIRSpec and the MRS, respectively.

3.1. *NIRSpec Fixed Slit Observations*

3.1.1. *PAHs and Related Spectral Features*

Figure 2 shows the spectra on the blue side of the NIRSpec detector gap for the seven objects observed in the Proto-PAH program. PAHs and PAH-like species dominate the spectra.

IRAS 05360 has a typical Class B PAH spectrum, with a strong 3.29 μm feature from aromatic C–H stretching modes outshining the weak aliphatic C–H stretching modes at 3.4 μm and beyond. In the Class D sources, the aliphatic C–H modes dominate, except for J004441, the D2 source in the SMC, where the aromatic and aliphatic emission peaks have similar strengths. These sources look much like similar carbon-rich post-AGB objects in the Galaxy (e.g., Geballe & van der Veen 1990).

The spectral resolution and sensitivity of NIRSpec separate the aliphatic emission complex into components centered at 3.43 and 3.50 μm more cleanly than possible in previous spectra of similar Galactic sources. Sandford et al. (1991) obtained laboratory spectra of short aliphatic hydrocarbon chains and found that the asymmetric and symmetric C–H stretches in methylene (CH_2) groups appear at 3.42 and 3.50 μm, respectively. Completely superhydrogenated PAHs (H_n-PAHs) produce similar spectral fea-

Table 2. Atomic and Molecular Inventory of the Proto-PAH Spectra

Line or Band	MSX SMC 029	SMP LMC 011	IRAS 05073	IRAS 06111	2MASS J004441	IRAS 05110	IRAS 05360
Class	C/abs	C	D1	D1	D2	D2	B
H I in NIRSpec	···	em	weak abs	weak abs	abs	abs	em
Forbidden lines	···	em	···	···	···	···	···
C_2H_2 3.0 μm	abs	abs/em:	abs	abs	abs	abs	abs
CH_4 3.3 μm	abs	em	···	···	···	···	abs
CO 4.7 μm	abs	em (P Cyg)	abs/em	abs/em	abs/em	abs/em	P Cyg
CN 4.8 μm	weak abs	weak em	weak em	weak em	em	em	···
HCN 7.0 μm	···	abs	abs	abs	abs	abs	abs
C_2H_2 7.5 μm	abs	abs	abs	abs	abs	abs	abs
C_4H_2 8.1 μm	abs	abs	abs	abs	abs	abs	abs
H_2 0–0 S(3) 9.66 μm	···	em	weak em	weak em	···	weak em	···
C_2H_4 10.5 μm	···	abs	···	···	···	···	abs
Unidentified 12.2 μm	abs	abs	abs	abs	abs	abs	abs
C_2H_2 12–15 μm	abs	abs	abs	abs	abs	abs	abs
Unidentified 14.31 μm	···	weak em	em	em	weak em	weak em	em
C_6H_6 14.85 μm	abs	abs	···	···	···	···	···
HC_3N 15.08 μm	abs	abs	···	···	···	···	···
C_4H_2 15.79 μm	abs	abs	weak em	weak em	···	weak abs	weak abs
C_4H_2 15.94 μm	abs	abs	P Cyg	P Cyg	abs	P Cyg	P Cyg
C_6H_2 16.09 μm	abs	abs	P Cyg	em	abs	P Cyg	abs
C_4H_2 16.26 μm	abs	weak abs	em	em	em	em	em
Unidentified 16.48 μm	···	···	em	em	···	weak em	em
CH_3 16.51 μm	abs	abs	···	···	···	···	abs
H_2 0–0 S(1) 17.03 μm	···	weak em	em	···	···	weak em	weak em
CH_3 17.63 μm	···	abs	···	···	···	···	abs
C_2H_2 20.0 μm	weak em	em:	em	em	weak em	weak em	em

NOTE—"em" = emission, "abs" = absorption, and "P Cyg" = P Cygni profiles. Colons mark uncertain identifications.

tures (Sandford et al. 2013). The corresponding stretches in methyl (CH_3) groups are shifted to shorter wavelengths, 3.38 and 3.48 μm (Sandford et al. 1991). Clark et al. (in prep.) have analyzed the aromatic and aliphatic C–H stretching modes more quantitatively, and Ricca et al. (in prep.) have generated computational modeling of potential carriers. Section 5.3 continues the discussion of the results of these combined efforts.

MSX SMC 029 and SMP LMC 011 show *absorption* from the aliphatic C–H stretches in the 3.4–3.6 μm range. In addition to the absorption, MSX SMC 029 also has an emission feature at 3.29 μm from aromatic C–H stretches. The structure of the absorption resembles the emission in the Class D sources, with strong components at 3.43 and 3.51 μm. The absorption sources have an additional component at 3.38 μm, which could arise either from H_n-PAHs (e.g., Bernstein et al. 1996; Sandford et al. 2013) or asymmetric C–H stretches in CH_3 groups (Sandford et al. 1991). Clark et al. (in prep.) are investigating this absorption more quantitatively.

The Galactic carbon-rich post-AGB object AFGL 618 also has a 3.4 μm absorption band (Lequeux & Jourdain de Muizon 1990; Chiar et al. 1998). Bernard-Salas et al. (2006) had previously noted the similarities in the spectra of SMP LMC 011 and AFGL 618 at longer wavelengths.

The spectral structure from the aliphatic PAH-related hydrocarbons at 3.4–3.5 μm shows additional structure from methane (CH_4), atomic lines, and a few unidentified lines or narrow bands, as discussed in the rest of Section 3.1. No other molecular spectral structure appears to be present, most notably from the CH_2 and CH_3 groups responsible for the broader structure. That missing molecular structure indicates

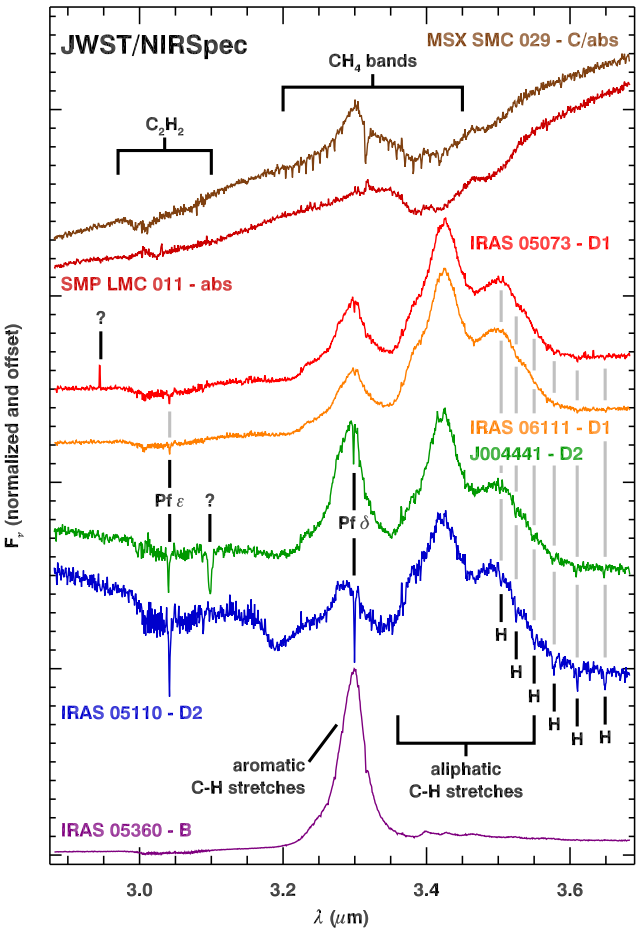

Figure 2. The 2.88–3.68 μm portion of the NIRSpec data for the seven objects in the Proto-PAH sample, with dust features, molecular bands, and atomic lines marked.

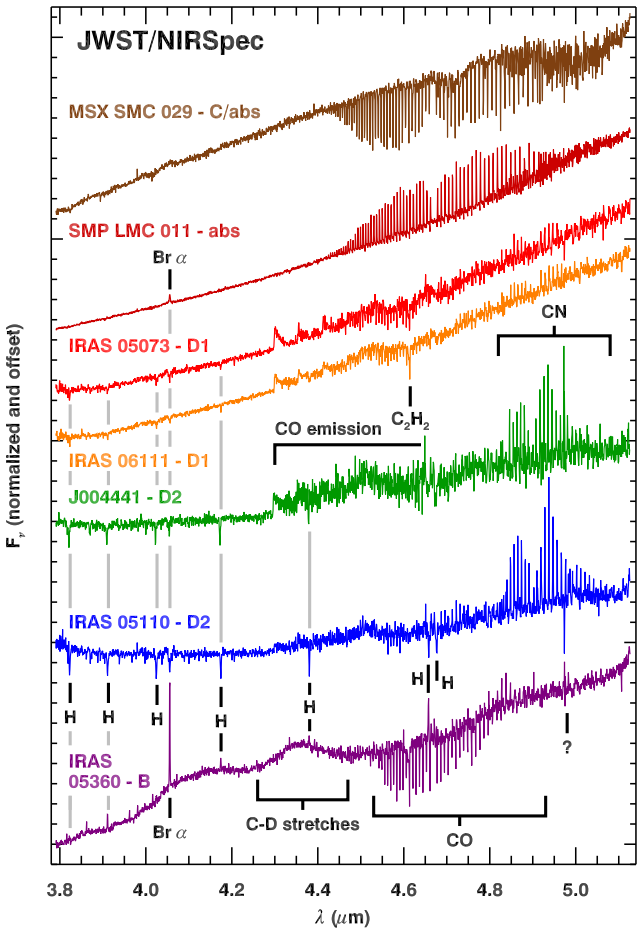

Figure 3. The 3.79–5.13 μm portion of the NIRSpec data for the seven objects in the Proto-PAH sample.

that CH_2 and CH_3 groups are attached to much larger aromatic skeletons and are not a family of smaller free-floating molecules.

In Figure 3, the spectrum of IRAS 05360 has a broad emission feature at 4.35 μm that has been attributed to an aromatic carbon–deuterium stretch analogous to the C–H stretch at 3.29 μm (e.g., Peeters et al. 2004; Misselt et al. 2025). The corresponding aliphatic feature at 4.7 μm does not appear to be present, although modeling of the CO absorption in this spectral region is needed to establish an upper limit. IRAS 05360 also shows an emission feature at 4.1 μm of unknown origin.

3.1.2. *Methane at 3.3 μm*

The spectrum of MSX SMC 029 has a comb of strong molecular absorption bands on top of the broad spectral features visible in Figure 2. We identify these bands as methane (CH_4). Figure 4 compares the methane absorption in MSX SMC 029 with the HITRAN2024 database (Gordon et al. 2026).[4] As the figure shows, methane absorption bands also appear in the spectrum of IRAS 05360. In SMP LMC 011, the methane band appears in *emission*. The Q branch at 3.31 μm is clearly present, as are several other bands at their expected wavelengths, although this spectrum also shows emission from other unidentified contributors.

Section 3.3 describes the determination of radial velocities. Work is underway on spectral analysis using synthetic spectra based on more realistic models (Das et al. in prep.).

3.1.3. *Acetylene at 3.0 μm*

Six of the seven spectra show the molecular absorption band at 2.95–3.10 μm from acetylene (C_2H_2). The exception is SMP LMC 011, where the data are more ambiguous and the band might be in partial emission. Acetylene absorption at 3.0 μm is well known in carbon stars (e.g., Ridgway et al. 1978; van Loon et al. 2008) and carbon-rich post-AGB objects (Chiar et al. 1998; Goto et al. 2003).

[4] Hereafter "HITRAN".

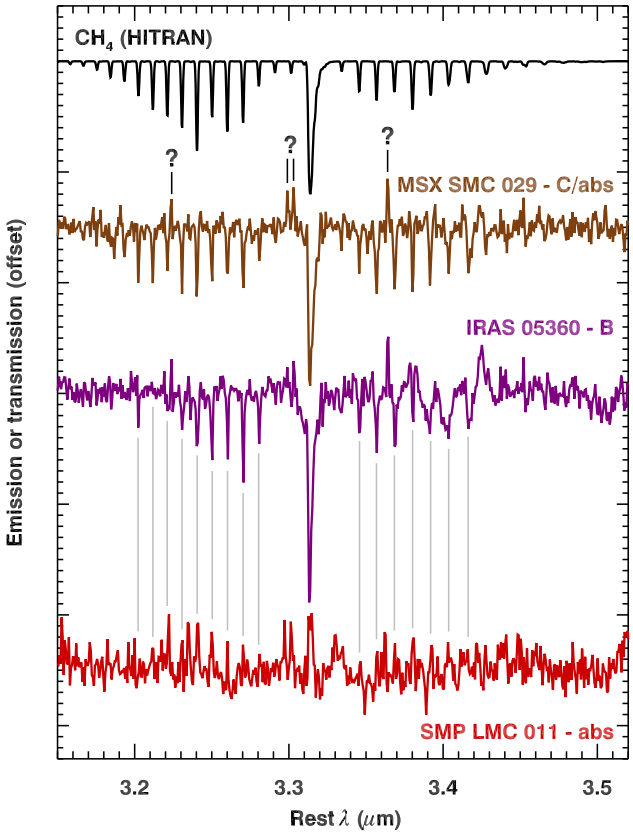

Figure 4. Methane bands at 3.3 μm, in absorption in MSX SMC 029 and IRAS 05360 and in emission in SMP LMC 011. The last spectrum includes emission bands from other unidentified contributors. The synthetic spectrum uses data from HITRAN2024 (Gordon et al. 2026). The continuum has been removed from the observed spectra, and they are corrected for radial velocity, as described in Section 3.3.

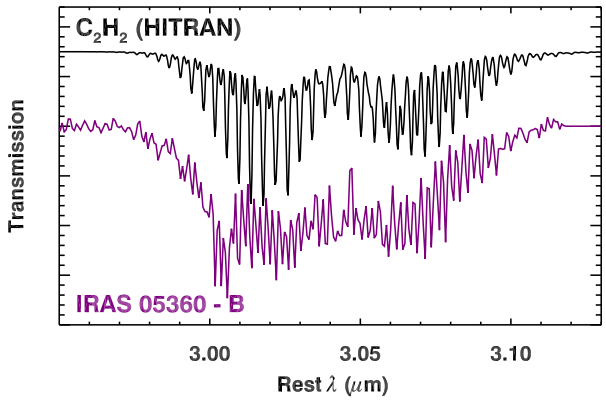

Figure 5. Acetylene absorption at 3.0 μm. The spectrum of IRAS 05360 is corrected for an estimated radial velocity of 229 km s^{-1}. The synthetic spectrum is from HITRAN2024 (Gordon et al. 2026).

Figure 5 compares a synthetic spectrum of acetylene based on HITRAN to the observed spectrum of IRAS 05360 after removing the continuum. The observed spectrum is shifted from a radial velocity of 229 km s^{-1} (see Section 3.3). The match is close to line-for-line on the red side of the band. On the blue side, the observed spectrum contains additional structure which may be from HCN (see Chiar et al. 1998; Goto et al. 2003).

3.1.4. *CO and CN*

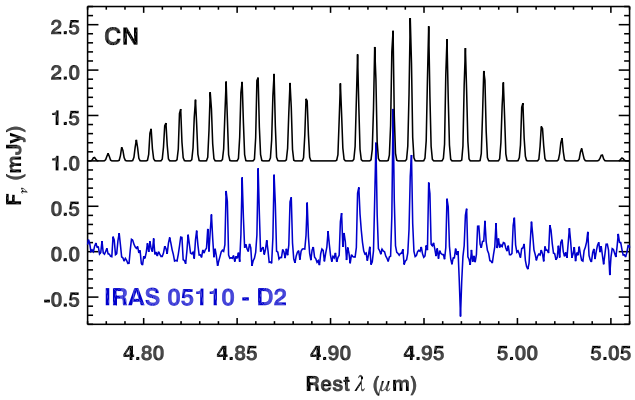

Figure 6. A simple model of CN compared to the continuum-subtracted spectrum of IRAS 05110, which has been corrected for a radial velocity of 240 km s^{-1}. The scaling of the model is arbitrary and is chosen for visual comparison. The absorption line at 4.97 μm is unidentified.

Figure 3 shows the red portion of the spectra from NIRSpec. Molecular emission and absorption from CO and CN dominate this wavelength range. The CN emission is moderately strong in the Class D2 sources and weaker in the Class D1 sources. CN also appears in emission in the spectrum of SMP LMC 011.

Figure 6 compares a synthetic spectrum from a simple model of CN to the observed spectrum of IRAS 05110. We have removed a continuum from the observed spectrum by subtracting a medianed spectrum using a 100 pixel boxcar and corrected for a 240 km s^{-1} radial velocity (as determined from the CN spectrum).

The CO band structure takes multiple forms in the spectra. It appears in absorption in MSX SMC 029 and in combinations of emission and absorption in the other six sources. In SMP LMC 011, all of the individual bands are in emission, but most show a weak blue-shifted absorption component which resembles the start of a P Cygni profile. In the Class B source IRAS 05360, the CO shifts from absorption at 4.5 μm to P Cygni profiles at ∼4.7 μm and to full emission beyond 4.8 μm. Each of the four Class D sources shows a mixture of CO emission and absorption, with strong bandheads in emission at ∼ 4.3–4.4 μm, which require dense CO heated to high temperatures.

This complex behavior mirrors what is seen in similar objects in the Galaxy. Hrivnak et al. (1994) observed the CO

overtone at 2.3 μm in 16 carbon-rich Galactic post-AGB objects and found emission in three. One object switched from emission to absorption in an interval of three months. Pukītis (2026) recently reported spectral variations in the CO in three similar Galactic objects.

3.1.5. *Atomic Hydrogen Lines*

The two Class D2 sources show absorption from atomic hydrogen in Figure 2 at 3.04 μm (Pfund ε), 3.30 μm (Pf δ), and in the 3.5–3.7 μm range, where six lines in the Humphreys series appear (the 6–24 to 6–19 transitions). The two D1 sources show the two Pfund lines and some of the Humphreys lines, but more weakly. The presence of these lines reveal that we have a direct line of sight to the central star or are seeing scattering from dust with a direct line of sight.

In Figure 3, IRAS 05360 and SMP LMC 011 both show Bracket α in emission at 4.05 μm, and IRAS 05360 shows four other hydrogen emission lines. All four Class D sources show the same lines in absorption, with other lines apparent as well. The hydrogen absorption is stronger in the Class D2 sources than the D1 sources, just as in the 3–4 μm range. Other hydrogen lines may be revealed by modeling the CO and CN band structure.

3.1.6. *Unidentified Features*

Several unidentified features appear in the spectra. J004441 has a strong absorption band at 3.10 μm not seen in the spectra of other sources and almost certainly not an artifact. This feature is not crystalline water ice, because it is too narrow and not accompanied by absorption at 6.2 μm. IRAS 05073 has an emission line at 2.944 μm which covers three wavelength elements, but we cannot rule out an artifact in this case. The notch in the spectra of the two Class D1 sources at 3.005 μm may be related to the acetylene absorption band.

Figure 4 has four unidentified lines not marked in Figure 2: at 3.225 μm; a pair at 3.299 and 3.303 μm; and 3.365 μm (at rest). The line at 3.299 μm in the velocity-corrected spectra in Figure 4 is not Pfund δ (3.297 μm), although it is close in the spectrum of SMP LMC 011, where it would require a radial velocity of 320 km s^{-1}, which is larger than any of the measured radial velocities from other bands and lines, 254–295 km s^{-1} (see Section 3.3). For MSX SMC 029, it would have a radial velocity of 306 km s^{-1}, compared to measured velocities of 116–138 km s^{-1}, and for IRAS 05360, 394 versus 207–256 km s^{-1}. The 3.225 μm line is close to H_2 (1,0) O(5) at 3.235 μm, but a match to this line would require a blueshift in the spectrum.

3.2. *MIRI MRS*

3.2.1. *The 5–11 μm Spectral Region*

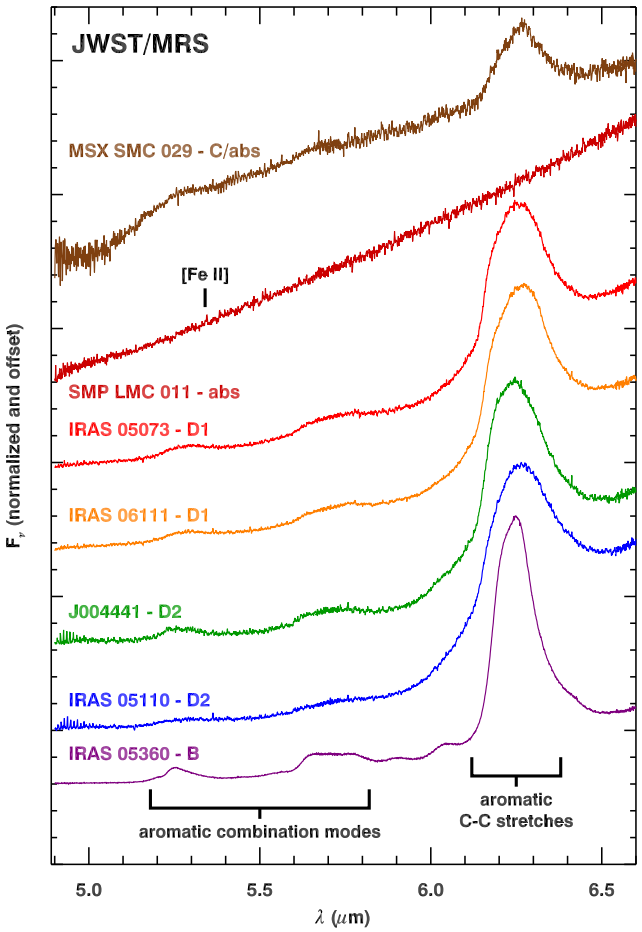

Figure 7. The 4.9–6.6 μm spectral region in the MRS data, which is dominated by the PAH features at 5.2, 5.7, and 6.2 μm. The red end of the CN emission comb is visible at 4.9 μm in the two Class D2 spectra.

Figures 7 and 8 show that broad emission features attributed to PAHs and related hydrocarbons dominate the MRS spectra below 9 μm. The aromatic features include the combination modes at 5.2 and 5.7 μm, the stronger features from C–C stretches peaking at 6.2 and 7.8 μm, and the C–H in-plane bending modes at 8.6 μm, with some overlap between the C–C and C–H modes. In the Class D1 and D2 spectra, strong aliphatic C–H modes at 6.9 and 7.3 accompany the aromatic features.

In class D1 and D2, a broad emission component fills the emission trough between 7.8 and 8.6 μm. Jensen et al. (2022) demonstrated the similarity of this additional component to the emission feature at ∼8.2 μm in Class C spectra by combining Class B and Class C spectra to closely mimic the Class D profiles emission at 7–9 μm as observed by the IRS. This approach does not work for the Class D spectra at 11–14 μm, but it does indicate that the extra emission compoment at 8–8.5 μm is related to Class C spectra. The physical nature of this component is not known, although it is likely related

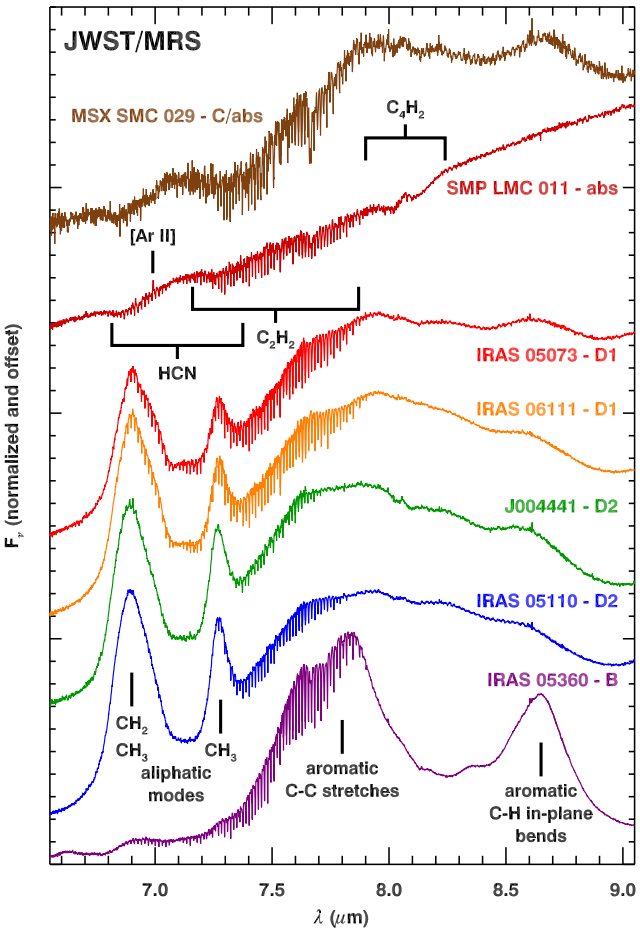

Figure 8. The 6.55–9.05 μm spectral region in the MRS data, showing the aliphatic C–H features at 6.9 and 7.3 μm and the PAH features peaking at 7.85 and 8.7 μm. The resolution of the MRS reveals a rich absorption spectrum from molecular bands, including methane and acetylene, overlaying the broad emission features.

to aliphatic hydrocarbons, because Class C in general is associated with a higher aliphatic/aromatic hydrocarbon ratio (Sloan et al. 2007; Pino et al. 2008).

All of the PAH and PAH-related features look similar to the lower-resolution spectra from the IRS, which is significant. The features from aliphatic methyl and methylene groups at 6.9 and 7.3 μm have not broken up into finer structure at higher resolution, as would be expected if they arose from small isolated molecules. Instead, these spectral features must arise from C–H bonds in aliphatic groups attached to large aromatic skeletons.

The most notable difference between the Spitzer spectra and the higher-resolution spectra from the MRS is the appearance of a manifold of molecular absorption bands from $\sim$6.9 to 7.9 μm. The band structure longward of $\sim$7.2 μm is absorption from acetylene, as seen in carbon stars (e.g., Aoki et al. 1998; Sloan et al. 2026). The absorption from 6.8 to 7.2 μm is from HCN (Aoki et al. 1998; Das et al. in prep.). Section 5.5 investigates how these bands affect measurements of the centroids of the PAH features in lower-resolution spectra.

All of the spectra except possibly IRAS 05360 have a shallow "W"-shaped absorption band centered at 8.1 μm identified as diacetylene (C_4H_2) by Das et al. (in prep.). It is strongest in the absorption spectra, weaker but clearly present in the Class D2 spectra, and weakest in the D1 spectra.

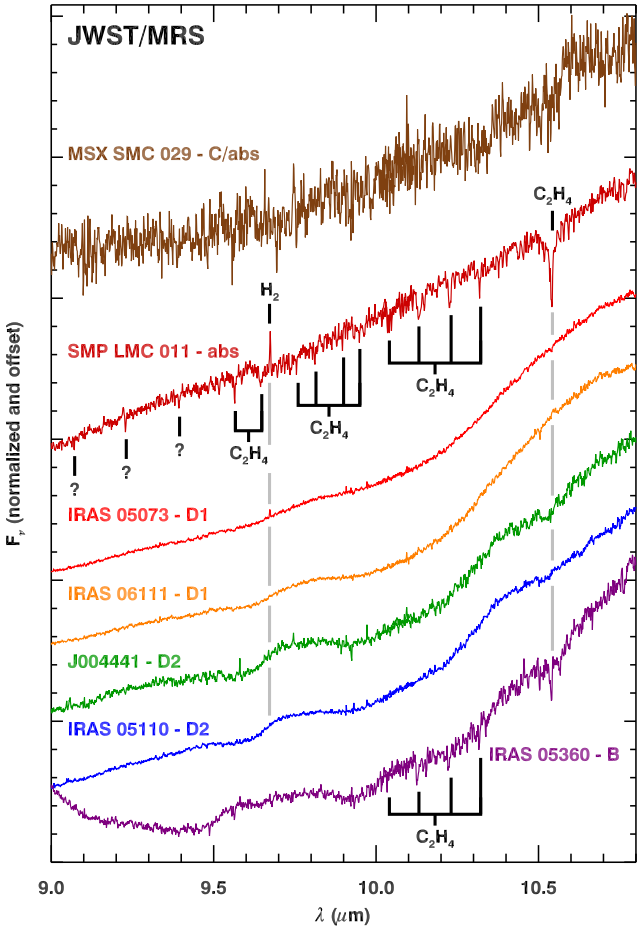

Figure 9. MRS spectra of the transition region at 9.0–10.8 μm between the PAH emission complexes at 7–9 and 11–14 μm. Ethylene absorption appears in two spectra, with the strongest band at 10.5 μm.

The spectrum of SMP LMC 011 has two forbidden lines in the 5–9 μm range. A weak [Fe II] line appears at 5.34 μm (Figure 7), and a stronger [Ar II] line appears at 6.99 μm (Figure 8). Several of the spectra show narrow weak features at 8.60 or 8.65 μm, but these appear to be artifacts.

Figure 9 plots the MRS spectra in the 9.0–10.8 μm region between the PAH and PAH-related emission features in the 6–9 and 11–14 μm regions. The strongest feature is the ethylene (C_2H_4) band at 10.5 μm, which Bernard-Salas et al. (2006) identified in Spitzer spectra of SMP LMC 011. Mod-

eling by Malek et al. (2012) confirmed its presence. A series of ten absorption bands from 9.5 to 10.3 μm also arise from ethylene (Das et al. in prep.). Additional bands marked as unidentified in Figure 9 may arise from ethylene, but that connection is unconfirmed. Several ethylene bands are visible in the spectrum of IRAS 05360.

The spectra of SMP LMC 011 show the H_2 0–0 S(3) line at 9.66 μm. This line appears more weakly in three of the four Class D spectra, all except J004441.

3.2.2. *The 11–15.4 μm Spectral Region*

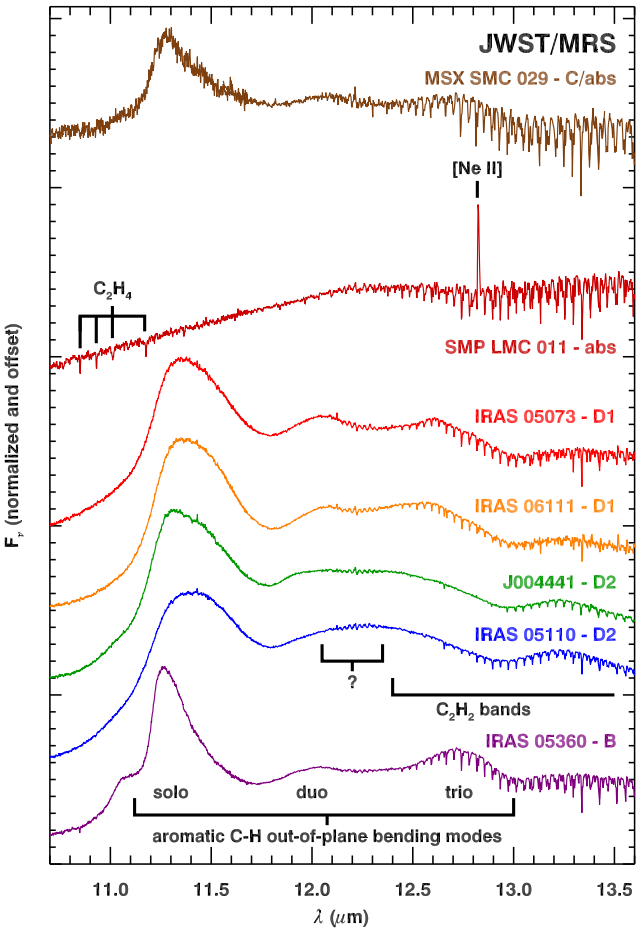

Figure 10. The 10.7–13.6 μm region in the MRS spectra, which is dominated by the aromatic C–H out-of-plane bending modes. Their differences define the Classes D1 and D2. In addition, acetylene absorption is prominent past ∼12.3 μm.

Figure 10 shows the 10.7–13.6 μm spectral region, which is dominated by aromatic out-of-plane bending modes. The Class B solo mode shows a blue outlier at 11.1 μm attributed to ionized PAHs by Sloan et al. (1999). The general appearance of the Class B, D1, and D2 spectra matches the Spitzer spectra fairly well, but some differences between the classes are now more clear. The Class D spectra show much wider features from the solo mode at 11.2 μm, and in the D2 spectra, an additional emission component is filling in the usual gap between the duo and trio modes at 12.0 and 12.7 μm, respectively. In the D1 spectra, the trio mode has shifted to the blue by ∼0.1 μm, and in the D2 spectra, a feature at ∼13.2 μm has replaced it. These differences define the D1 and D2 classes (Sloan et al. 2014).

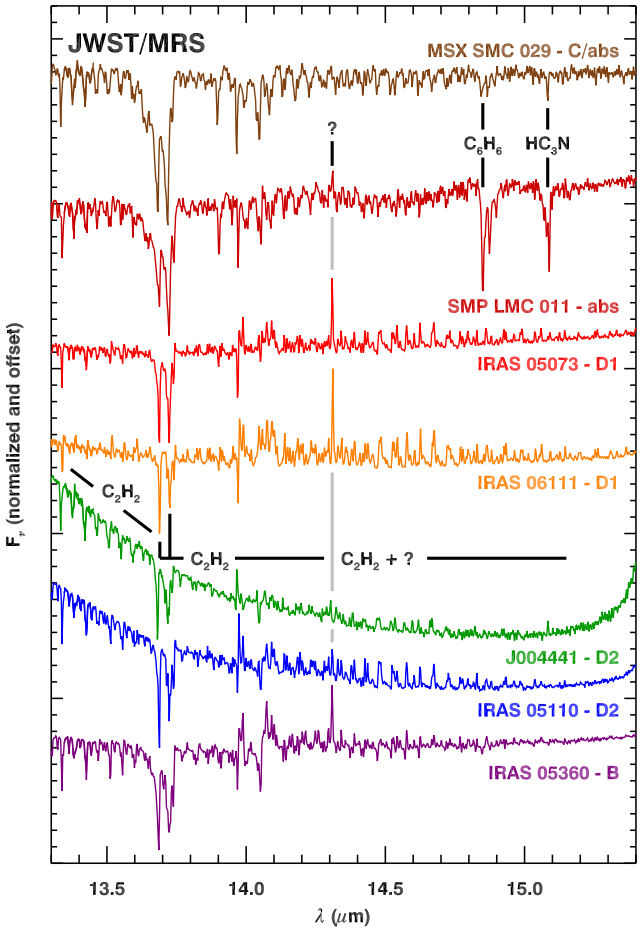

Figure 11. MRS spectra of The 13.3–15.4 μm spectral region, showing the rich hydrocarbon absorption spectrum dominated by acetylene (C_2H_2), most notably at 13.7 μm, with contributions from other molecules labeled. Except for the two absorption sources, the molecular band structure goes into emission to the red of 13.9 μm.

Molecular absorption bands hidden at the lower resolution of the Spitzer spectra are now visible as in the 6–9 μm region. The acetylene absorption dominates, but another band at ∼12.0–12.34 μm is apparent. This new unidentified band does not arise from fringing, because it shifts with radial velocity in the spectrum of J004441 compared to the LMC sources.

SMP LMC 011 has a strong [Ne II] line at 12.81 μm and (at least) four more ethylene absorption bands near 11 μm.

Bernard-Salas et al. (2006) previously noted the absorption at 11.1 μm but did not identify the carrier.

Figure 11 displays the acetylene-dominated region of the spectra between 13.3 and 15.4 μm. Acetylene is responsible for the strong double-peaked absorption at 13.7 μm from the Q branch of the ν_5 transition. The P and R branches extend to either side. HCN is likely to be present, but that requires verification with modeling, which will be challenging due to the presence of acetylene in both emission and absorption. The HCN ν_2 band at 14.01 μm identified by Cernicharo et al. (2001) in AFGL 618 does not appear to be present in the Proto-PAH sample. In both D1 sources, some of the acetylene bands are in emission starting at 13.5 μm, and they grow strong past 13.9 μm. The D2 sources and IRAS 05360 also show emission past 13.9 μm.

In addition to acetylene, the two absorption sources show clear absorption band complexes from benzene (C_6H_6 ν_4) at 14.85 μm and cyanoacetylene (HC_3N ν_5) at 15.08 μm. Cernicharo et al. (2001) identified these bands in the spectrum of AFGL 618, and Bernard-Salas et al. (2006) identified them in Spitzer spectra of SMP LMC 011. Now they have also been identified in MSX SMC 029, although they are weaker than in the other sources (Das et al. in prep.).

An emission line (or band) appears at 14.311 μm in the spectrum of SMP LMC 011, both Class D1 sources, and IRAS 05360. The line is not from [Ne V] (14.322 μm) or [Cl II] (14.368 μm), as those would require radial velocities of -230 and -1190 km s^{-1}, respectively. Its carrier is unknown.

3.2.3. *The 15–18 μm spectral region*

Figure 12 continues the wavelength coverage of the MRS data to 15.2–17.8 μm. It shows numerous molecular bands in emission and absorption. The diacetylene (C_4H_2 ν_8) transition at 15.94 μm dominates, along with a nearby weaker absorption band from triacetylene (C_6H_2 ν_{11}) at 16.09 μm. Cernicharo et al. (2001) identified both of these bands in spectra from AFGL 618 and the Cygnus Egg, and Bernard-Salas et al. (2006) identified them in Spitzer spectra of SMP LMC 011. The MRS spectra confirm the presence of additional diacetylene bands identified or suggested in the spectrum of SMP LMC 011 at 15.79 and 16.26 μm by Malek et al. (2012), who noted that propyne ($CH_3C{\equiv}CH$) could also contribute at 15.79 μm. Cernicharo et al. (2001) identified cyanodiacetylene (HC_5N ν_7) at 15.58 μm in the spectrum of AFGL 618, but it does not appear in SMP LMC 011.

J. Li et al. (2026) have identified the methyl radical (CH_3) in the spectrum of SMP LMC 011 at 16.51 and 17.63 μm. Its presence indicates a significant deviation from the expected chemistry. Three of the Class D spectra and IRAS 05360 have an emission feature at 16.48 μm. While close to the CH_3 band, it arises from an unknown carrier.

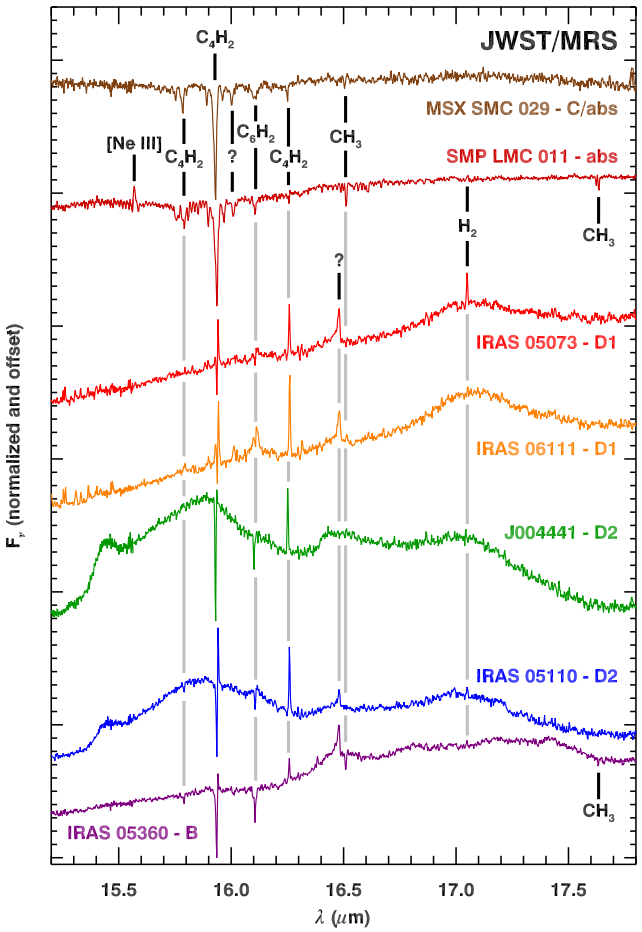

Figure 12. The 15.2–17.8 μm spectral region in the MRS data, showing all of the spectra have emission and/or absorption from simple hydrocarbon molecules. The identification of CH_3 is new (J. Li et al. 2026). The Class D2 spectra show dust emission features with peaks at 15.4, 15.8, 16.4, and 17.1 μm, while the Class D1 spectra just show the feature at 17.1 μm.

The spectrum of MSX SMC 029 also shows most of the same spectral features in this wavelength range as SMP LMC 011, except for the absence of both the 17.63 μm CH_3 band and the [Ne III] line at 15.56 μm. While MSX SMC 029 does not have any forbidden emission lines in its spectrum and SMP LMC 011 does not show PAH-like material in emission, the two sources otherwise have remarkably similar spectra. See Das et al. (in prep.) for further analysis.

IRAS 05360 also shows absorption from CH_3 at 16.51 and 17.63 μm, indicating that the unusual chemistry seen in SMP LMC 011 is not unique to the absorption sources in the sample.

Figure 13 focuses on the 15.94 μm band from diacetylene in the Class D and B sources. Four of the five spectra have a P Cygni profile, while in J004441, the red emission

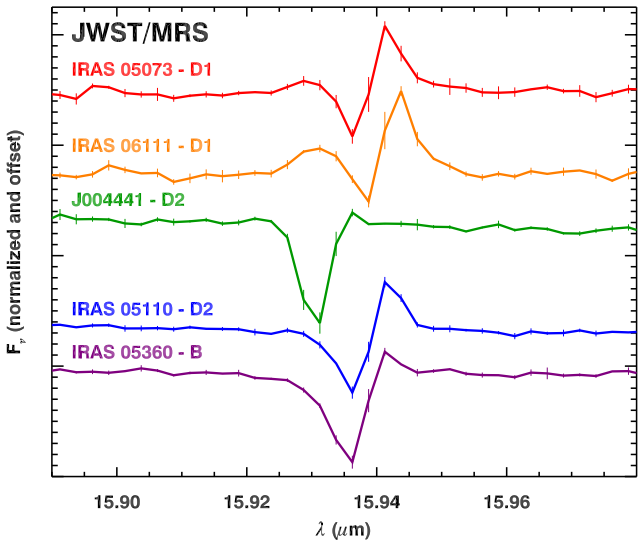

Figure 13. A close-up of the C_4H_2 band at 15.94 μm in the Class B and D spectra. The bottom two spectra have P Cygni profiles with blue-shifted absorption, while the top two show asymmetric self-absorbed emission profiles. J004441 shows only a weak emission component. These spectra appear at their observed wavelengths, showing the difference in radial velocity for the sole SMC source, J004441.

component is much weaker than in the other sources. Thus, we are seeing an absorbing component moving toward us in the outflows from these objects. In the D1 sources, the absorption is weaker, making the profiles look more like self-absorbed emission. In MSX SMC 029 and SMP LMC 011, the 15.94 μm bands are entirely in absorption, as are the diacetylene bands at 15.79 and 16.26 μm. The 15.79 μm band appears in four of the other five spectra (except for J004441), either in emission or absorption, while the 16.26 μm appears in emission in all five.

All five of the Class D and B spectra have absorption from triacetylene at 16.09 μm, but with unusual profiles in the Class D spectra. The spectrum of IRAS 05360 has a P Cygni profile, as do both of the D2 sources. In IRAS 06111, the 16.09 μm band is part of an emission complex.

Figure 12 also shows broad and smooth emission features centered roughly at 15.4, 15.8, 16.4, and 17.1 μm in most of the spectra. As with the aliphatic modes at 3.4–3.5, 6.9 and 7.3 μm, in the higher-resolution MRS spectra, the features still have a broad and smooth appearance. The features at 15.4 and 15.8 μm are more distinct compared to the Spitzer spectra, as is the feature at 16.4 μm. The juxtaposition of this last feature with the unidentified molecular emission at 16.48 μm is interesting. Whether or not the molecular bands and dust features in this wavelength region are physically related is an open question.

The H_2 0–0 S(1) line appears at 17.03 μm in four of the spectra, three of which also show the S(3) line at 9.66 μm (see Table 2). The S(2) and S(4) lines at 12.28 and 8.03 μm are not visible. The odd J transitions arise from orthohydrogen, while the even transitions are from parahydrogen. The missing S(2) and S(4) lines imply a high ortho/para ratio, but modeling of the other molecules around these lines is needed before upper limits for these lines can be determined. The ortho/para ratio approaches 3 for high densities ($n_H > 10^4$ cm^{-3}) and can exceed this value if the orthohydrogen can self-shield (Draine & Bertoldi 1996).

3.2.4. *The 18–23 μm spectral region*

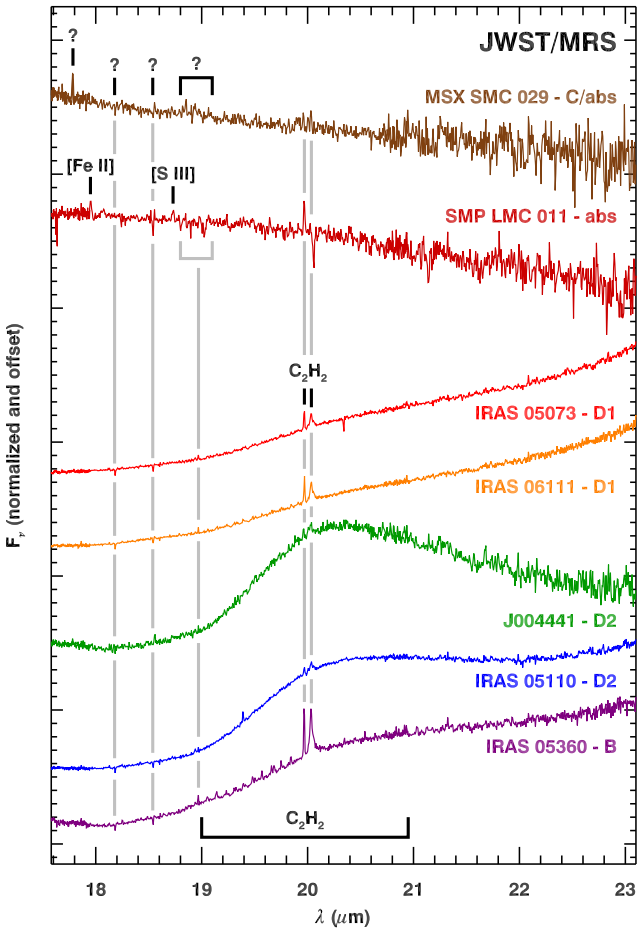

Figure 14. The MRS spectra at 18–23 μm, showing the 21 μm feature, acetylene emission centered at 20 μm, and several unidentified bands. Acetylene produces the two narrow bands at 20 μm and the satellite features extending 1 μm to either side, as Figure 15 shows.

Figure 14 shows the MRS spectra from 18 to 23 μm. The 21 μm emission feature (which is actually centered at 20 μm) dominates this spectral region in the two Class D2 sources and is noticeable in IRAS 05360 as well. It is present, but more subtle, in the two D1 sources. The larger sample of D1 and D2 sources considered by Sloan et al. (2014) show similar behavior.

All of the spectra show two narrow emission bands at 19.97 and 20.04 μm, most prominently in IRAS 05360 and the two Class D1 sources. The 20.04 μm band is clearly broader than the 19.97 μm band. The bands are weaker in the D2 sources and possibly not present in MSX SMC 029. SMP LMC 011 shows the 19.97 μm band in emission along with an absorption band at 20.06 μm that may be related or may be from a different carrier.

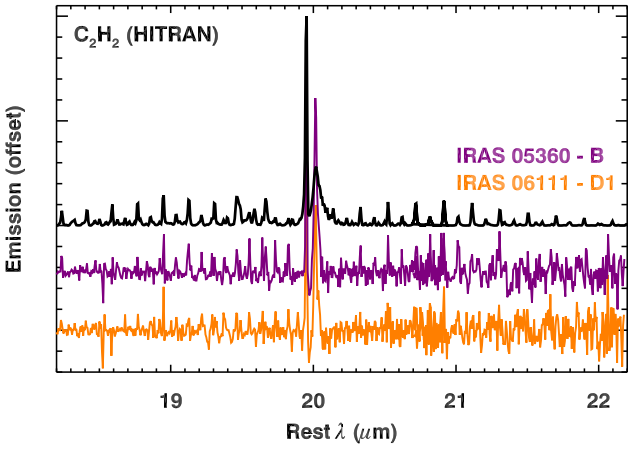

Figure 15. A synthetic spectrum of acetylene compared to the observed emission structure at 20 μm in two sources. The positions of the two dominant bands at 19.95 μm and 20.02 μm and the weaker bands to either side identify acetylene as the carrier. The spectra of IRAS 05360 and IRAS 06111 have been corrected for radial velocities of 256 and 298 km s^{-1}, respectively, based on the position of the narrow band at 19.95 μm (Section 3.3).

Figure 15 compares a synthetic spectrum of acetylene from the HITRAN database to two observed spectra and shows that the narrow emission bands at ~19–21 μm arise from acetylene gas. In addition to the two strong bands at 19.95 and 20.02 μm, acetylene produces several weaker bands which reproduce the observed spectra of both IRAS 05360 and IRAS 06111. As with the HITRAN-based comparison to methane at 3.3 μm, this synthetic spectrum is meant for identification purposes. The relative strengths of the 19.95 and 20.02 μm bands in the synthetic spectrum differ considerably from the observations, and the satellite bands to either side show different structures as well. These differences tell us that the observed emitting gas probably arises from physical conditions somewhat different from the Earth's atmosphere. Bhatt et al. (in preparation) have analyzed the acetylene emission with better models.

SMP LMC 011 has two forbidden lines in Figure 14, [Fe II] at 17.95 μm and [S III] at 18.73 μm. Both are weak, but they are at the correct wavelengths (see Section 3.3).

Figure 14 marks several unidentified bands. MSX SMC 029 has an emission band at 17.79 μm which does not appear in the other sources. This band is in the overlap region between MRS Bands 3C and 4A (segments 8 and 9), appears clearly in both, and covers several pixels, leading to the conclusion that it is real. The emission complex at 18.8–19.1 μm in MSX SMC 029 also appears to be real. The spectrum of SMP LMC 011 shows possible structure at these wavelengths as well. Four of the seven spectra show two clear absorption bands at 18.18 and 18.54 μm. Some of the other spectra may have these bands as well, but in the two SMC sources, the 18.54 μm band is in emission. The Class D and B spectra show an emission band at 18.97 μm. As Figure 15 shows, this band is close to an acetylene emission band, but its unusual strength raises the possibility that another carrier is responsible.

Two apparent absorption bands not marked in Figure 14 appear to be artifacts, at 19.39 μm in IRAS 05110 and 20.38 μm in IRAS 05073. They both cover only two pixels and are associated with larger uncertainties.

Table 3. Atomic Radial Velocities in SMP LMC 011

Line	Expected Wavelength (μm)	Observed Wavelength (μm)	Radial Velocity[a] (km s^{-1})
Br α	4.0523	4.0557 ± 0.0002	254 ± 15
[Fe II]	5.3402	5.3448 ± 0.0006	259 ± 31
[Ar II]	6.9853	6.9916 ± 0.0004	273 ± 16
[Ne II]	12.8136	12.8256 ± 0.0002	282 ± 6
[Ne III]	15.5551	15.5703 ± 0.0012	292 ± 23
[Fe II]	17.9360	17.9533 ± 0.0047	290 ± 78
[S III]	18.7130	18.7300 ± 0.0037	276 ± 59

[a] The radial velocity determined in the optical is 263.5 km s^{-1} (Morgan & Parker 1998). See Section 3.3 for an explanation of the uncertainties.

3.3. *Radial Velocities*

The radial velocities of different features, atomic and molecular, can provide evidence of kinematic structures including disks and outflows that otherwise cannot be probed in these unresolved targets.

The spectrum of SMP LMC 011 contains Br α emission at 4.05 μm and a number of forbidden emission lines in the MRS portion. For each line, we fit a linear continuum underneath it and measured the line position by (1) fitting a gaussian, and (2) integrating from either side to find the (interpolated) wavelength that bisects the total flux in the line. Table 3 presents the mean of these two measurements. The uncertainty is the larger of the uncertainty in the mean of these two measurements or the uncertainty in the integrated

Table 4. Radial Velocities from Atomic Hydrogen

Target	Class	Lines Measured	Lines Used	Radial Velocity (km s^{-1})[a]
IRAS 05073	D1	12	8	237 ± 5
IRAS 06111	D1	14	6	276 ± 3
J004441	D2	14	10	128 ± 4
IRAS 05110	D2	16	10	251 ± 4
IRAS 05360	B	5	3	249 ± 3

[a] Uncertainties are the uncertainty in the mean.

position, which accounts for the uncertainty in the continuum.

The radial velocity of SMP LMC 011 based on optical emission lines is 263.5 km s^{-1} (Morgan & Parker 1998). The positions of the lines up to 7 μm are consistent with that measurement, but the lines at longer wavelengths show higher velocities. The [Ne II] line is strong, has a clean profile, and is not consistent with the optical radial velocity. The velocity of the [Ne III] line is also inconsistent with the optical value, although its position is less certain. The two longest-wavelength lines have large uncertainties due to the uncertainty in the fitted continuum.

Table 4 gives estimated radial velocities for the five sources with multiple atomic lines. The line positions were determined as for the lines in SMP LMC 011. The "Lines Measured" column counts the lines which could be seen in the spectra, but some lines were affected by possible blends or noise in the continuum to either side. Those were excluded from the final count, as were lines with a S/N < 3.0.

Table 5 combines the radial velocities from Tables 3 and 4 with the results for H_2, three acetylene bands, one methane band, and CO.

The radial velocities for H_2 are based on the lines measured in five sources (see Table 5). The uncertainties are the uncertainties in the mean of the two lines where they were available. The larger uncertainties are for the two sources with just one line and are calculated as described for the forbidden lines in SMP LMC 011 above.

We measured radial velocities from the C_2H_2 band at 3.0 μm by first isolating the observed transmission spectrum and then finding the radial velocity that minimized the differences when compared to a synthetic spectrum from HITRAN. We divided the observed spectrum by a linear continuum to either side of the absorption band. We normalized the synthetic spectrum to the observed spectrum, and then measured the χ^2 residuals in steps of 1 km s^{-1}. The quoted radial velocity corresponds to the minimum residuals. The result for SMP LMC 011 is more uncertain because the band may be in partial emission.

This method requires some caveats. First, the HITRAN line strengths are directly from the database and are applicable to the Earth's atmosphere, which is unlikely to be close to either the temperature or density of the absorbing gas in the Proto-PAH sources. Changes in these quantities will change the relative band strengths and are likely to shift the apparent band centers. Second, we are examining C_2H_2 in isolation and not considering isotopologues or other molecules, which could add bands to the observed spectrum and shift the results. Third, the systematics in this approach lead to a high floor to the residuals, so that the minimum χ^2 should not be used to estimate the uncertainties. Consequently, we have not provided uncertainties for the determined velocities. We estimate that they are on the order of ± 15 km s^{-1}.

The measured radial velocities for the CH_4 band at 3.3 μm followed the same approach as the C_2H_2 band at 3.0 μm, but the "continuum" required a different treatment. In this case the spectrum underlying the molecular absorption bands is dust-like emission from aromatic and aliphatic C–H stretches. To estimate its "continuum", we fitted a spline to the spectra between the individual CH_4 bands. The methane appears in only three of the seven spectra. In SMP LMC 011, it is in emission, so we subtracted the continuum instead of divided by it. Its spectrum is noisier or contains structure from other molecules, making its radial velocity more uncertain. Table 5 gives the resulting radial velocities; they were used to shift the spectra in Figure 4.

For the CO, we measured each detected line between 4.44 and 4.90 μm and compared the position to the corresponding line for the v=1–0 transition (using HITRAN as the reference). MSX SMC 029 had 57 absorption lines in that range, and we excluded six due to blends or noise. For SMP LMC 011 also had 57 lines, but in emission, and we excluded two. Many of the lines in SMP LMC 011 exhibited a weak blue-shifted absorption compoment which may have pushed our measured radial velocities to slightly higher values. As noted in Section 3.1.4, the CO band structure in IRAS 05360 shows more complexity, with lines in emission, with P Cygni profiles, and in absorption. A few other lines were noisy. We measured 37 lines and kept 22 of them, all in absorption. The CO band structure in the Class D sources is even more complex and would require modeling for a proper determination of radial velocity. The uncertainties in Table 5 are standard deviations. The uncertainties in the mean are 1 km s^{-1} in all three cases, which is probably less than the systematic errors from our simplified approach.

Table 5. Combined Radial Velocities

Target	Class	Radial Velocity (km/s)						
		Atomic Lines	H_2 Lines	C_2H_2 3.0 μm	CH_4 3.3 μm	CO 4.7 μm	C_2H_2 7–8 μm	C_2H_2 20 μm
MSX SMC 029	C/abs	···	···	116	123	114 ± 6	138	···
SMP LMC 011	abs	254–292	284 ± 5	206:	296	295 ± 5	265	273 ± 31
IRAS 05073	D1	237 ± 5	255 ± 1	242	···	···	243	265 ± 11
IRAS 06111	D1	276 ± 3	305 ± 25	284	···	···	284	298 ± 10
J004441	D2	128 ± 4	···	113	···	···	134	173 ± 43
IRAS 05110	D2	251 ± 4	257 ± 6	246	···	···	255	276 ± 35
IRAS 05360	B	249 ± 3	236 ± 32	229	207	214 ± 6	236	256 ± 6

NOTE—Uncertainties are uncertainties in the mean for atomic hydrogen. See Section 3.3 for the remaining uncertainties. Where uncertainties are not given, we estimate them to be $\sim$15 km s^{-1}. A colon indicates an uncertain measurement.

The analysis of the C_2H_2 band at 7–8 μm follows the same approach as the CH_4, using a spline to estimate the continuum from the underlying PAH-related emission, comparing the continuum-corrected spectrum to the HITRAN spectrum, and iterating through radial velocities to find the minimum residuals. The acetylene appears in absorption in all seven spectra, although it it noisier in the two SMC sources. Generally, other molecules appear to be contributing to the absorption in this spectral region.

To measure the radial velocity of the C_2H_2 emission at 20 μm, we took a different approach. Because only two of the seven spectra in the sample show the secondary emission bands covering the 19–21 μm range, we concentrated on the narrow emission band at 19.85 μm. It appears to be unresolved by the MRS. In the HITRAN spectrum, it has a central wavelength of 19.9503 ± 0.0003 μm. The band can be measured in six of the seven spectra, and for those, we used the same approach described for the forbidden lines in SMP LMC 011 to measure the line center and the uncertainty.

These radial velocities should be considered preliminary given all of the caveats for the analysis of the molecular bands and the uncertainties in the measurements. Nonetheless, the data hint that different lines and bands may show real differences in radial velocity. For example, they could be tracing different physical components in an unresolved source with a complex geometry including a central disk or torus, outflows, and an extended dust shell. Amorphous carbon is the dominant absorber at all wavelengths, and its opacity falls roughly as wavelength squared. As a result, the parts of the system visible in the near-infrared could differ significantly from those visible at longer wavelengths. That all these components share the same radial velocity seems unlikely.

4. ADDITIONAL DATA

Rich survey data from other space missions can supplement the spectra from JWST and Spitzer and help build a more complete picture of the nature of the Proto-PAH sample.

4.1. *Light Curves*

The Wide-field Infrared Survey Explorer (WISE) (Wright et al. 2010) provides multi-epoch photometry between the epochs of the cold Spitzer mission and JWST. The cryogenic WISE mission, the Near-Earth Object WISE (NEOWISE) phase (Mainzer et al. 2011), and the NEOWISE-Reactivated (NEOWISE-R) mission (Mainzer et al. 2014) cover the periods 2010 to 2011 and 2014 to 2024. The epochs are spaced roughly six months apart and include photometry at 3.4 μm (W1) and 4.6 μm (W2).

For each of our targets, we downloaded photometry from the NASA/IPAC Infrared Science Archive.[5] We used the AllWISE Multi-epoch Photometry Table and the NEOWISE-R Single Exposure (L1b) Source Table. Sloan et al. (2026) described how the data from individual scans are combined to a median magnitude and uncertainty in the mean for each epoch.

Figure 16 presents the results. The two absorption sources show unmistakable temporal variations in the last two decades between the Spitzer and JWST spectroscopy.

[5] http://irsa.ipac.caltech.edu

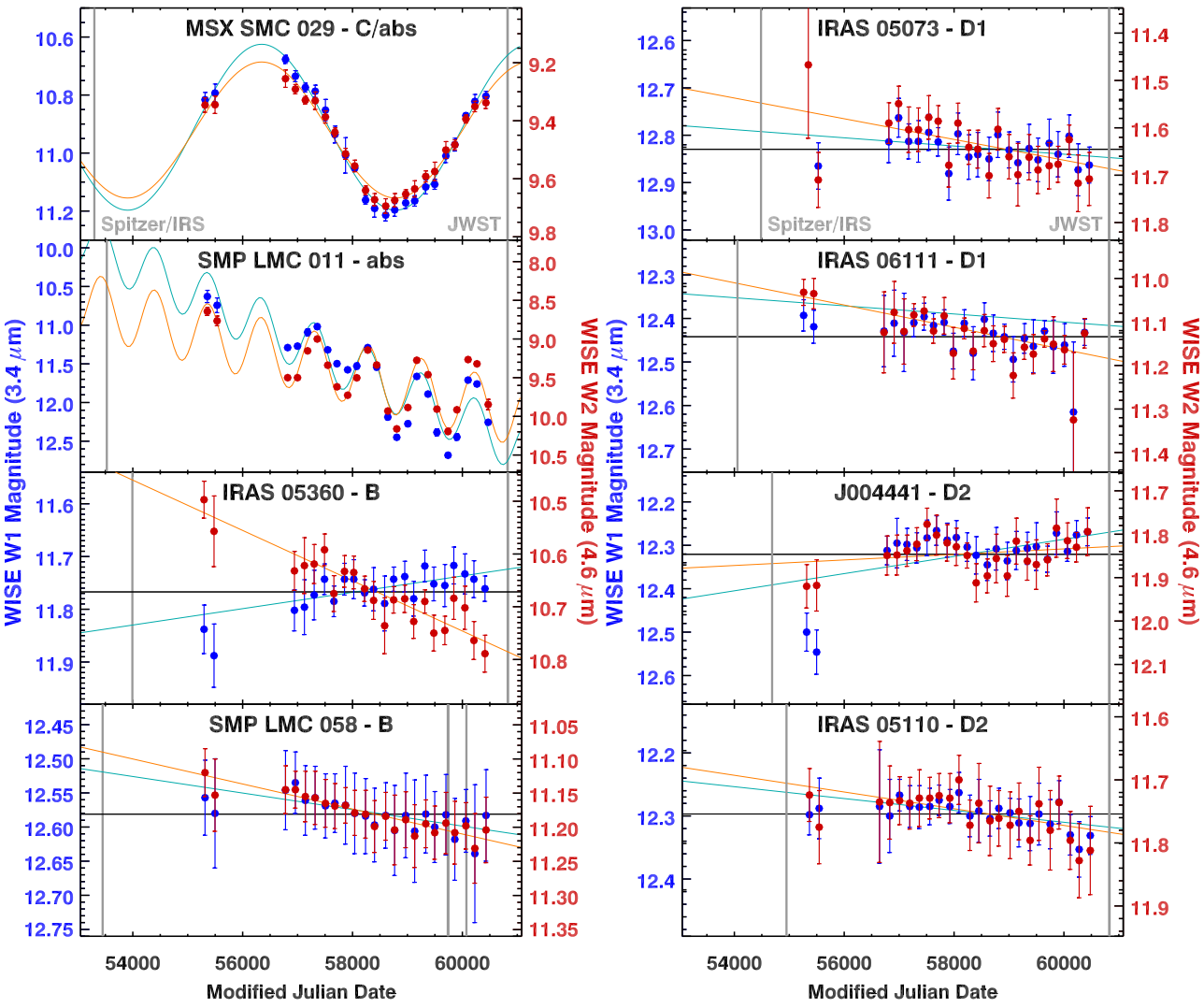

Figure 16. Multi-epoch photometry from WISE for the Proto-PAH sample and SMP LMC 058. The error bars indicate the uncertainties in the mean for each epoch. The vertical gray lines mark the spectroscopic observational epochs, with the Spitzer/IRS epochs on the left and the JWST epochs on the right. The horizontal lines give the mean magnitudes, and the colored lines and curves give the fitted light curves for W1 (orange) and W2 (light blue), as Section 4.1 explains. Tables 6 and 7 provide the parameters for the fitted lines and periodic behavior, respectively.

SMP LMC 011 has dimmed by roughly a magnitude, with periodic variations superimposed, while MSX SMC 029 shows only periodic changes. We fitted lines to the trends in all of the sources except MSX SMC 029, and Table 6 gives the results. Table 7 provides the results of our analysis of periodic behavior in MSX SMC 029 and SMP LMC 011. We fitted periods and amplitudes using the method described by Sloan et al. (2026, their appendix A). The uncertainties in both tables are 1-σ.

MSX SMC 029 can be fitted with a period of 4880 days, or 13.4 y. Table 7 shows that the results for the two WISE filters fitted separately agree to within 35 days. The peak-to-peak amplitudes are ∼0.5–0.6 magnitudes. The changes in overall brightness in the MIR spectrum are consistent with the fitted lightcurve, with the IRS observation coming near minimum and the JWST observations near maximum. The changes in the brightness of the spectrum are smaller at longer wavelengths, where cooler dust further from the center of the system would dominate more than at shorter wavelengths.

SMP LMC 011 has faded in brightness over the course of the extended WISE mission, modulated by a cyclic variation with a period of ∼970 days. Fitting the W1 and W2 lightcurves separately gives periods which differ by 44 days, or 4.5% of the total period. Uncertainty in the fitted linear decline contributes to the discrepancy, but it is not the full story. A close look at the light curve reveals that the amplitude of the variations may be increasing with time. While we have fitted a line to the underlying light curve for the time-

Table 6. Linear Trends in the Light Curves

	Coefficients of Fitted Lines			
	W1 (3.4 μm)		W2 (4.6 μm)	
	at MJD 53000	Slope	at MJD 53000	Slope
Target	(mag)	(10^{-5} mag/d)	(mag)	(10^{-5} mag/d)
MSX SMC 029[a]	10.911 ± 0.005	···	9.432 ± 0.005	···
SMP LMC 011	10.051 ± 0.314	29.98 ± 0.540	11.144 ± 0.245	10.03 ± 0.419
IRAS 05073	12.780 ± 0.441	0.865 ± 0.755	12.699 ± 0.453	2.186 ± 0.775
IRAS 06111	12.375 ± 0.347	0.934 ± 0.594	12.292 ± 0.309	2.552 ± 0.529
J004441	12.424 ± 0.334	-1.980 ± 0.570	12.353 ± 0.409	-0.638 ± 0.700
IRAS 05110	12.244 ± 0.307	0.940 ± 0.527	12.223 ± 0.425	1.325 ± 0.730
IRAS 05360	11.846 ± 0.351	-1.552 ± 0.599	11.507 ± 0.343	4.767 ± 0.586
SMP LMC 058	12.514 ± 0.521	1.211 ± 0.894	12.482 ± 0.350	1.832 ± 0.602

[a] The magnitudes for MSX SMC 029 are mean magnitudes based on fitting a sinusoid to the light curve.

Table 7. Periodic Behavior in the Light Curves

	Period		Mean	Zero-phase	Peak-to-peak Amplitude	
	W1	W2	Period	Epoch	W1	W2
Target	(d)	(d)	(d)	(MJD)	(mag)	(mag)
MSX SMC 029	4898	4863	4880 ± 18	56346 ± 9	0.573	0.468
SMP LMC 011	989	955	972 ± 17	55370 ± 6	0.695	0.821

frame considered, it is possible that WISE has only caught some portion of a longer cyclic variation.

The remaining panels in Figure 16 have a horizontal line marking the mean magnitude in both W1 and W2. The error bars are uncertainties in the mean. Typically, each epoch had ∼55 individual measurements, so the standard deviation of the data within an epoch would be ∼7.5 times larger than what is shown in the figures. In the majority of the panels, all or most of the error bars overlap or approach the mean magnitude, and in Table 6, the fitted slopes are usually below 3-σ and not statistically significant. Four targets show a slight decline in brightness that may or may not be real: SMP LMC 058, IRAS 05073, IRAS 06111, and IRAS 05110. The spectra in Figure 1 are mostly consistent with a possible decline in brightness between the IRS and JWST epochs, most notably for SMP LMC 058, and least for IRAS 05073. In none of these four cases is the MRS spectrum brighter than the IRS.

Two other sources show potentially interesting behavior. The photometry of IRAS 05360 indicates that it may be growing bluer in time in the 3–5 μm range. The negative slope for W2 is an 8-σ result. However, the blue end of the IRS and MRS data suggest that the source is growing fainter, not brighter. The lightcurve of J004441 is dominated by a possible rise in brightness to MJD ∼ 57500 and then a drop to ∼ 58500, but the variations are not much larger than the uncertainties.

4.2. *Spectral Energy Distributions*

Figure 17 presents the spectral energy distributions (SEDs) of the sample. The data include spectra from Gaia DR3 (Gaia Collaboration 2016, 2023) covering 0.336–1.02 μm and SPHEREx (Bock et al. 2026)[6] covering 0.74–5.01 μm. Figure 17 also includes photometry from VizieR (Ochsenbein et al. 2000) via Simbad (Wenger et al. 2000) based on searches with a 1″ radius.

[6] The Spectro-Photometer for the History of the Universe, Epoch of Reionization and ices Explorer.

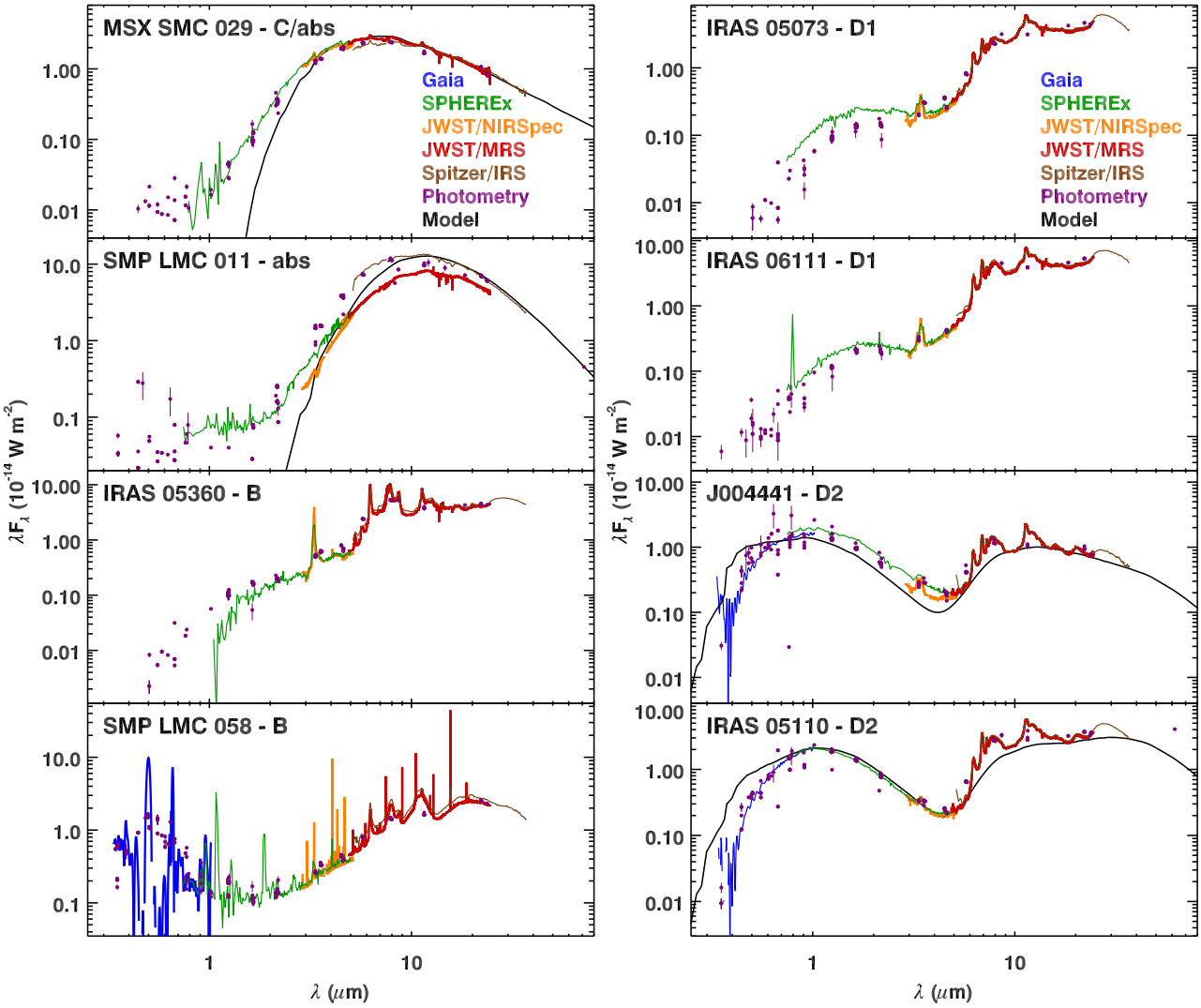

Figure 17. SEDs of the sample constructed from available spectroscopy from JWST, Spitzer, Gaia, and SPHEREx and photometry via VizieR. The plotted MRS spectra exclude Band 4C (beyond 24 μm) due to the poor S/N. For four sources (MSX SMC 029, SMP LMC 011, J004441, and IRAS 05110), the results of a spherically symmetric model are included (see Section 4.2).

The SEDs of the Class D2 and D1 sources differ, with the D2 sources showing a much stronger optical/NIR component. This component is weaker in the D1 sources, and even weaker in the Class B source IRAS 05360. The other Class B source, SMP LMC 058, shows a UV/optical excess expected for a more mature PN with an exposed white dwarf at its center. The two absorption sources are deeply embedded within optically thick dust shells.

4.3. *Luminosities*

For measuring luminosities and radiative-transfer modeling, we modified the SEDs in Figure 17 by shifting the IRS spectrum down ∼10% to match the MRS, except for the two sources found to be variable (MSX SMC 029 and SMP LMC 011). We did not use the MRS data longward of 27 μm. The SPHEREx data overlap the NIRSpec data from 3 to 5 μm and for the four spectra that did not agree, we scaled SPHEREx to NIRSpec.[7] The Gaia data were scaled with the SPHEREx data, with one exception.[8]

We determined total fluxes by integrating the modified SEDs and correcting for interstellar extinction. We assumed an average A_V in the LMC of 0.55 mag based on the NIR photometric analysis of Zaritsky et al. (2004). For the SMC, we assumed half that value. The extinction curve used to correct for reddening is from Rieke & Lebofsky (1985), except that we modified the shape of the 10 and 18 μm silicate absorption based on our own analysis of spectra from IRAS.

[7] The multiplicative corrections to SPEHREx were 0.95 for MSX SMC 029, 0.58 for SMP LMC 011, 0.83 for IRAS 05073, and 0.75 for J004441.

[8] For J004441, the Gaia spectrum was scaled by a factor of 0.90 to match SPHEREx.

MSX SMC 029 and SMP LMC 011 show significant variability between the Spitzer and JWST epochs, and for those two, we calculated rough minimum and maximum luminosities. For SMP LMC 011, the minimum spectrum was created by combining the JWST spectroscopy with the SPHEREx spectrum and the Spitzer values at longer wavelengths scaled by a factor of 0.753. The maximum spectrum was created from the Spitzer spectrum with the SPHEREx data scaled by a factor of 2.2 to match. For MSX SMC 029 the spectrum at minimum light was created from the Spitzer spectrum, with the SPHEREx data scaled by a factor of 0.752 to match. The maximum spectrum was based on the SPHEREx and JWST data with the Spitzer spectra used beyond 27 μm and scaled to the MRS at that wavelength.

To determine luminosities, we scaled the integrated fluxes to the assumed distances of the LMC and SMC, 50.0 and 62.4 kpc, respectively (Pietrzyński et al. 2019; Graczyk et al. 2020). Table 8 shows the results.

4.4. *Radiative-Transfer Modeling*

We fitted one-dimensional radiative-transfer models to the SEDs to explore how well a spherically symmetric model could fit the data. This effort uses the DUSTCD code (Leung 1975, 1976). The dust was assumed to be the amorphous carbon BE1 grains from Rouleau & Martin (1991) with a radius of 0.1 μm. The modeling requires specification of the spectral shape of the central star's radiation field, its luminosity, the inner radius of the shell (or equivalently the dust temperature at the inner radius), the the outer radius of the shell, the optical depth at a reference wavelength, and the density distribution over the radial range.

The starting luminosity of the star is assumed to be 8240 $L_\odot$. Ultimately, the luminosity is scaled based on the distance. The spectral shape uses Kurucz models (Castelli & Kurucz 2003) for T_* and $\log_{10}(g)$ based on the spectral type and similar information available for the star. Lacking that, we assumed T_* = 6500 K and $\log_{10} g$ = 0.0, suitable for an F-type supergiant. We assumed a power law for the density profile: $\rho(r) = \rho_0(r_{\rm in}/r)^\alpha$ out to an outer radius usually, $\sim$0.8 pc. When a single shell with a simple density power law failed to fit the long-wavelength shape of the SED, we added a discrete thin shell, increasing the density by a factor N at a specific radius $r_{\rm shell}$. The models are calculated for a distance to the object d of 1 kpc. Comparing the flux density of the model to the observed values provides a scaling of the ratio L_*/d^2. We fitted a grid of models over the parameters (α, r_{in}, τ at 11.22 μm, and optionally N plus $r_{\rm shell}$) and then used a least-squares matching of models to the photometry or spectroscopy of the source at a set number of wavelengths with a scaling factor.[9]

To estimate the strength of the 21 and 30 μm features, we empirically determined templates for the feature profiles and added them to the base amorphous carbon dust properties, as described by Volk et al. (2011). The shape of the 30 μm feature varies among sources (e.g., Hony et al. 2002), and we used three possible templates for this feature with different peak wavelengths in the 27–33 μm range. Two of the profiles were derived from the spectra of carbon stars while the third profile was derived from the spectra of carbon-rich post-AGB objects.

The models of the two absorption sources, SMP LMC 011 and MSX SMC 029, started with a stellar template based on the spectrum of the carbon star T Lyr (K. Volk, private communication). At the high optical depths of these models, the shape of the stellar continuum makes negligible differences to the output spectrum.

The radiative transfer code generated models that agreed reasonably well with the observed data for four objects in the sample, the two absorption sources and the two Class D2 sources. Figure 17 includes model spectra for those four cases. Table 9 provides the parameters of the best-fitting models. These results form the basis for the discussion in the next section. For the four objects where a model did not work, the Class D1 and B sources, it is likely that the geometry of the circumstellar dust deviates significantly from spherical symmetry.

5. DISCUSSION

5.1. *The Absorption Sources*

Radiative transfer modeling can fit the MIR emission of both absorption sources with spherical shells, but the observed optical and NIR excesses compared to the models point to possible deviations from spherical symmetry. The light curves (Section 4.1) offer indirect evidence that both sources might be binaries.

For MSX SMC 029, a variability period of 13.4 y is too long for stellar pulsation and even long secondary periods. This period suggests an orbital origin. A companion star would have to orbit *inside* the dust shell; otherwise, we would see an optical/NIR peak in the SED. We could be seeing heating of the near side of the dust shell when the secondary passes close to our line of sight to the carbon star.

For SMP LMC 011, a period of 972 d combined with a peak-to-peak amplitude at 4.6 μm of 0.82 mag points to Mira-like pulsations. Its luminosity is consistent with

[9] The optical depth at V is 141 times that at 11.22 μm.

Table 8. Fluxes and Luminosities

Target	Phase	Class	Total Flux	Dereddened Flux	Luminosity
			(10^{-14} W m^{-2})	(10^{-14} W m^{-2})	($L_\odot$)
MSX SMC 029	minimum	C/abs	4.19	4.23	5130
MSX SMC 029	maximum	C/abs	4.71	4.76	5770
SMP LMC 011	minimum	abs	12.1	12.3	9550
SMP LMC 011	maximum	abs	19.5	19.9	15470
IRAS 05073		D1	6.99	7.10	5530
IRAS 06111		D1	8.80	8.95	6970
J004441		D2	3.86	4.44	5390
IRAS 05110		D2	8.27	8.79	6840
IRAS 05360		B	8.70	8.82	6870
SMP LMC 058		B	4.75	5.44	4240

Table 9. Parameters for Successful Radiative Transfer Models

Target	$r_{\rm in}$	$T(r_{\rm in})$	α	τ (11.22 μm)	T_*	$R_{\rm shell}$	N
	(AU)	(K)			(K)	(AU)	
MSX SMC 029	15	1002	1.55	0.41	···	···	···
SMP LMC 011	68	538	2.24	0.8	···	···	···
J004441	780	283	2.30	0.008	6250	20,200	398
IRAS 05110	1220	254	3.5	0.024	6000	12,000	2820

its pulsation period. While pulsation periods $>$ 900 d are rare, Groenewegen & Sloan (2018) document eight cases in the sample of carbon stars in the LMC observed by the Spitzer/IRS. These objects differ by having much larger peak-to-peak amplitudes, $\sim$1.4–2.1 mag at 4.6 μm. The amplitude of SMP LMC 011 more closely resembles those of objects identified by Gruendl et al. (2009) as extreme carbon stars and by Sloan et al. (2016) as carbon-rich objects evolving off the AGB. Its highly reddened spectrum is also similar to those objects, but they usually show absorption from SiC dust (Speck et al. 1997), while SMP LMC 011 does not.

This characterization of SMP LMC 011 as an object near the end of its lifetime on the AGB contradicts conclusions based on previous observations. Imaging from the Hubble Space Telescope shows a compact bipolar structure analogous to AFGL 618, consistent with a post-AGB object (Shaw et al. 2006). Its optical spectrum shows hydrogen emission lines and low-ionization forbidden lines, from which Leisy & Dennefeld (2006) found a gas temperature of 20,800–29,100 K from [N II] and [O III], indicating an object closer to a PN.

One possible scenario is that SMP LMC 011 is a binary with a forming PN surrounded by a compact H II region and a still-pulsing carbon-rich object, with both components inside a carbon-rich dust shell beginning to lose its spherical symmetry. The general apparent decline in the brightness of the system could arise from a long orbital period. Given the short lifetime of the PN phase, this hypothesis would require two stars of almost exactly the same mass, with one emerging as a white dwarf and the other in the last stages of evolution on the AGB. That would be a very rare scenario. In addition, the total luminosity of the system at minimum is low for two stars at the end of their AGB lifetime.

Another possible scenario is a system with an extreme carbon star and a symbiotic nova companion. SMP LMC 011 has shown nebular emission for over 50 years since its discovery by Sanduleak et al. (1978). The ratio of emission from [O III] at 4959 and 5007 Å to Hβ rose by a factor of $\sim$3 in the time between observations by Morgan & Parker (1998) and Shaw et al. (2006). That behavior brings to mind systems like V1016 Cyg, a long-lived symbiotic nova system with multiple recorded outbusts (see the discussion by Arkhipova et al. 2015).

Both absorption sources have similar SEDs and can be fitted reasonably well with spherically symmetric radiative-transfer models. In both cases, some optical radiation from the central source is escaping the system, probably via scattered light. The infrared spectra are dominated by strong absorption bands from aliphatic hydrocarbons ranging from simple molecules (e.g., C_2H_2) to the larger particles responsible for the broad absorption at 3.4–3.5, 6.9, and 7.3 μm.

Despite those similarities, the infrared spectra of SMP LMC 011 and MSX SMC 029 show striking differences. SMP LMC 011 has emission from multiple forbidden lines as well as Br α at 4.05 μm, suggesting a source well on its way from the AGB to a PN, and yet its spectrum is remarkably free from any PAH emission features as seen in the rest of the sample. Their absence is difficult to explain. MSX SMC 029 has PAH emission features, but no atomic emission lines, which reverses what is seen in SMP LMC 011. The behavior of some of the molecular bands in the NIR is reversed in the two sources, with absorption from CH_4 at 3.3 μm and CO at 4–5 μm in MSX SMC 029, while SMP LMC 011 shows those two bands in emission.

The nature of the two absorption sources and the cause of the differences between them remain mysteries. Further work to understand the targets themselves is essential for putting the wealth of molecular detail in their spectra into context.

5.2. *The Class D1 and D2 Sources*

The differences in the positions of the out-of-plane C–H bending modes at 11–14 μm distinguish Class D1 from Class D2 sources. The two classes differ in other ways, even though those differences were not used to classify them. The sample considered by Sloan et al. (2014) had 10 Class D PAH sources based on the emission at 7–9 μm, including 4 Class D1 spectra and 6 Class D2 spectra. The broad 21 μm emission feature was weak or absent in the D1 spectra and strong in the D2 spectra. The SEDs also differed, with a more double-peaked SED due to a clearer optical path to the central source in the D2 sources. These differences are readily apparent in Figure 17.

The stronger optical emission from the Class D2 sources makes it possible to analyze the spectra from the central stars. IRAS 05110 has a spectral type of F3 II(e), according to van Aarle et al. (2011), whose modeling gave T_{eff} = 7000 K. Szczerba et al. (2020) determined a spectral type of F0 Ib for this object, which corresponds to T_{eff} = 6750 K. For J004441, De Smedt et al. (2011) estimated T_{eff} = 6250 K. Thus, both of the Class D2 sources in the present sample have evolved away from the AGB but are far from PNe. Optical spectral types for the D1 sources are not available, probably due to the higher optical depth of the dust and a more obscured central object. All four Class D sources have hydrogen absorption lines in their NIR spectra, with stronger absorption in the D2 spectra than in the D1 spectra.

The radiative transfer models (Section 4.4) provide indirect evidence that Class D1 and D2 sources deviate from spherical symmetry. The SEDs of the two Class D1 sources have a faint optical/NIR component that the models cannot fit. It is likely that a nonspherical morphology is needed, which suggests a disk or torus. Spherical models can fit the SEDs of the Class D2 sources, but with some caveats. First, the models overpredict the optical emission in the systems, suggesting an additional dust component obscuring the central star, such as a disk or torus. Second, the model of IRAS 05110 actually requires two shells to fit the flattened peak in the MIR. The need for a second shell in the model could alternatively be caused by a disk or torus in the object.

All of this evidence, while indirect, points to a bipolar symmetry like what is seen in Galactic analogs such as the Cygnus Egg and AFGL 618. With that geometry in mind, two potential explanations follow for the different SEDs in Class D1 and D2. First, the difference could be evolutionary, with the central sources in the D2 systems more exposed because they are more evolved. Alternatively, the differences between D1 and D2 could be an inclination effect, with the D1 sources more edge-on so that dust can better obscure the central regions in the system.

Either scenario explains the differences in the emission from the PAHs and PAH-like carbonaceous material in the two classes as due to different amounts of photo-processing. In both cases, the emitting material we are observing in the Class D2 sources has a clearer line of sight to a source of harsher radiation.

5.3. *Aromatics and Aliphatics in the Class D Spectra*

Laboratory spectroscopy of aliphatic hydrocarbons has considered simple free-standing aliphatic chains (e.g., Sandford et al. 1991), methyl sidegroups on PAHs (e.g., Joblin et al. 1996), and H_n-PAHs (e.g., Bernstein et al. 1996; Sandford et al. 2013; Demyk et al. 2026). At 3.4–3.5 μm, the picture is consistent with more photoprocessing in the Class D2 spectra. In the Class D spectra, the dominant stretching modes arise from methylene (CH_2) groups. Methyl (CH_3) groups also contribute in this spectral range, but the analysis by Clark et al. (in prep.) shows that the CH_2 contribution is stronger and that the CH_2/CH_3 ratio is lower in the Class D2 spectra than in Class D1. If the CH_2 and CH_3 groups arise in short aliphatic chains, then it follows that the photo-processing has eroded the chains to shorter lengths in the Class D2 spectra. While some of the emission from the CH_2 groups can arise from H_n-PAHs, the presence of emission components from CH_3 groups at 3.48 and 7.3 μm require

that some of the aliphatic hydrocarbon must be in some other form.

A comparison of the Class D spectra to laboratory spectra at 6.9–7.3 μm does not lead to the same conclusion as at 3.4–3.5 μm. Sandford et al. (2013) investigated the spectral properties of CH_2 groups in H_n-PAHs and find that the position of the 6.9 μm feature depends on the proximity of a CH_2 group to the aromatic skeleton. The multi-component spectral analysis by Clark et al. (in prep.) reveals that the CH_2 groups need to be adjacent to the aromatic skeleton and not in longer chains.

Computer simulations of mixed aliphatic and aromatic structures give a more consistent explanation of the spectral behavior. The simulations of hydrocarbons with 130 carbon atoms by Ricca et al. (in prep.) show that attached sidegroups and short chains reproduce the D2 spectra well at 3.3–3.5 μm and reasonably well at 6.9 and 7.3 μm.

The observed spectra show that in the out-of-plane C–H bending region (11–14 μm), the duo and trio modes have learly changed in Class D2 from their nominal positions. Clark et al. (in prep.) quantify these differences as well as the broadening of the 11.2 μm solo mode. They attribute these characteristics of Class D spectra to perturbations of the out-of-plane bending modes by aliphatic hydrocarbons. The simulations by Ricca et al. (in prep.) support this explanation. The current simulations do not match the observed spectra exactly, but they show that the observations can constrain the aliphatic/aromatic ratio.

At 15–18 μm, the MRS spectra show clear differences between the Class D1 and D2 spectra for which we do not have an explanation (Figure 12). All four of the Class D sources have an emission feature centered at 17.1 μm, but the D1 sources show no other emission features from PAH-like or dust-like material in this wavelength range. In the D2 sources, a strong emission feature at $\sim$15.8 μm has appeared, along with a shoulder at 15.4 μm that was not detected in the lower S/N spectra from Spitzer. Sloan et al. (2014) suggested that the 15.8 and 17.1 μm features seen in previous Spitzer spectra could arise from alkyne chains, possibly attached to PAHs, but the improved MRS spectra do not provide any additional evidence for that hypothesis.

5.4. *IRAS 05360*

IRAS 05360 has a Class B PAH spectrum like the PN SMP LMC 058, but the JWST spectra of the two sources differ dramatically. The evidence shows that IRAS 05360 is not a PN. The MRS spectrum of SMP LMC 058 has $\sim$50 emission lines, including forbidden lines, H I, and H_2 (Jones et al. 2023). The NIRSpec spectrum appears to be just as rich, with over 80 lines between 2.9 and 5.2 μm. IRAS 05360, on the other hand, shows only a handful of H emission lines in NIRSpec and one weak H_2 line in the MRS. The ionized region inside IRAS 05360 appears to still be deeply embedded within the circumstellar dust shell, and yet we can see Class B PAH emission, indicating that we can see carbonaceous material with a direct line of sight to the core of the object.

Like the absorption and Class D sources, IRAS 05360 shows a rich molecular spectrum from species including C_2H_2, CO, HCN, C_4H_2, and C_6H_2 (see Table 2). Unlike the Class D sources, IRAS 05360 also has CH_4 absorption at 3.3 μm, C_2H_4 absorption centered at 10.5 μm, and CH_3 absorption at 16.5 and 17.6 μm. SMP LMC 011 and/or MSX SMC 029 have those bands.

In short, IRAS 05360 shares some properties with the absorption sources, some with the Class D sources, and few with SMP LMC 058, the other Class B PAH source. Its unique properties challenge any attempt to place Class B, D1, D2, C, and strong molecular absorption into a common evolutionary sequence.

5.5. *The Effect of Molecular Bands on Feature Wavelengths*

The PAH classes have proven very useful, but they are qualitative. Measuring the central wavelengths of PAH emission features quantifies their shape and position (e.g., Sloan et al. 2007). The central wavelength (λ_C) is defined to bisect the total flux in an emission feature. The JWST spectra show the PAH features can be overlaid by strong molecular bands. That raises a question. How much do the previously unresolved molecular bands shift the measured centers of the features?

To answer that question, we focus on IRAS 05360 and the impact of C_2H_2 on the center of the 7–9 μm PAH complex. This object offers a worst-case scenario because the C_2H_2 is strong and the underlying feature is narrow, so that more of the wavelengths involved are affected by the absorption. Following Sloan et al. (2014), we removed the C–H in-plane bending mode at 8.6 μm (along with the accompanying 8.3 μm bump) by fitting and subtracting a line to the data in the intervals 8.21–8.33 and 8.82–8.94 μm. We then subtracted a linear continuum based on the intervals 6.65–6.74 and 9.00–9.12 μm and integrated the difference from 6.74 to 9.00 μm.[10] We measured the 7–9 μm complex in the observed spectrum and in a spectrum modified to remove the absorption bands. This latter spectrum was constructed by fitting a spline to the maxima between the individual absorption bands from HCN and acetylene from 6.8 to 7.9 μm.

The difference between the measured central wavelengths is 0.014 μm. In the observed JWST spectrum of IRAS 05360, λ_C = 7.807 $\pm$ 0.001 μm, compared to 7.821 $\pm$ 0.001 μm in the corrected spectrum. For comparison, Sloan et al. (2014) measured λ_C = 7.84 $\pm$ 0.01 μm with Spitzer. The reported uncertainties in their sample ranged from 0.01 to 0.08 μm, or

[10] These wavelength stops are from Sloan et al. (2014, Table 10).

generally larger than the 0.014 μm shift caused by the acetylene. The 7–9 μm PAH complex peaks at $\sim$7.65 μm in Class A, $\sim$7.85 μm in Class B, and $>$ 8.0 μm in Class C and D, making the effect of the molecular-band absorption $\sim$10% or less of the shifts between classes.

6. SUMMARY

The JWST spectra of seven carbon-rich post-AGB objects in the Magellanic Clouds reveal a wealth of new information about a key stage of evolution as stars become PNe and the observed dust changes from amorphous carbon into PAHs. The sample includes one source with Class B PAH emission typical for carbon-rich PNe, two sources each with Class D1 and Class D2 emission, and two sources with a rich molecular absorption spectrum, one of which also shows Class C PAH emission.

NIRSpec provides our first look in the 3–5 μm range at moderate spectral resolution and reveals the C–H stretching region from PAHs and aliphatic hydrocarbons. All four Class D sources show strong emission from aliphatics at 3.43 and 3.51 μm, while the two absorption sources show the aliphatics in absorption. The NIRSpec spectra also reveal hydrogen in absorption in the Class D sources, especially D2, and in emission in the Class B source and one of the absorption sources. The spectra can show emission or absorption, sometimes both, from C_2H_2 (acetylene) at 3.0 μm, CH_4 (methane) at 3.3 μm, CO centered at 4.7 μm, and CN centered at 4.9 μm. The CO shows P Cygni profiles in some cases.

The MRS spectra show a rich variety of molecular bands, mostly in absorption Most of the spectra show P Cygni profiles in the C_4H_2 (diacetylene) band at 15.94 μm, and some also show the same profile in the nearby C_6H_2 (triacetylene) band at 16.11 μm. All of the spectra show emission from C_2H_2 (acetylene) at 20 μm. The two absorption sources show even richer molecular content, with C_6H_6 (benzene), HC_4N, and even the methyl radical (CH_3), which also appears in the spectrum of the Class B source.

These spectra provide a wealth of clues about the chemistry of the gas and the molecular composition of the dust in this phase of stellar evolution critical to understanding how PAHs form from carbon-rich dust. This paper is designed to provide an overview of the targets and spectra. Additional papers investigating the spectra in detail are already submitted or in preparation.

G.C.S. and G.M.W. were supported as part of this observing program by STScI through grant JWST-GO-04678.001-A. H.L.D., R.S., N.C.S., and K.E.K. were similarly supported through JWST-GO-04678.002-A, 003-A, 007-A, and 008-A, respectively. H.L.D. also acknowledges supoort from NSF AST-2307117. N.C., E.P., J.C., C.B., and D.D. acknowledge support from the Canadian Space Agency (CSA, 24JWGO3B01), and the Natural Sciences and Engineering Research Council of Canada. J.C. and E.P. acknowledge support from the University of Western Ontario, the Institute for Earth and Space Exploration, and the Natural Sciences and Engineering Research Council of Canada. A.R. acknowledges support from the Internal Scientist Funding Model (ISFM) Laboratory Astrophysics Directed Work

Facilities: JWST (NIRSpec), JWST (MIRI), Spitzer Space Telescope (IRS), SPHEREx, Gaia

REFERENCES

Allamandola, L. J., Tielens, A. G. G. M., & Barker, J. R. 1985, ApJL, 290, L25

Allamandola, L. J., Tielens,

Aoki, W., Tsuji, T., & Ohnaka, K. 1998, A&A, 340, 222

Argyriou, I., Glasse, A., Law, D. R., et al. 2023, A&A, 675, A111

Arkhipova, V. P., Taranova, O. G., Ikonnikov, N. P., et al. 2015, Astron. Lett., 41, 613

Beichman, C. A., Neugebauer, G., Habing, H., et al. 1988, *Infrared Astronomical Satellite (IRAS) Catalogs and Atlases. Volume 1: Explanatory Supplement*

Bernard-Salas, J., Peeter, E., Sloan, G. C., et al. 2006, ApJL, 652, L29

Bernstein, M. P., Sandford, S. A., & Allamandola, L. J. 1996, ApJL, 472, L127

Bhatt, C., et al. 2026, in preparation

Bock, J. J., Aboobaker, A. M., Adamo, J., et al., 2026, ApJ, 999, 139

Böker, T., Beck, T. L., Birkmann, S. M., et al. 2023, PASP, 135, 38001

Brandl, B. R., Bernard-Salas, J., Spoon, H. W. W., et al. 2006, ApJ, 653, 1129

Bushouse, H., Eisenhammer, J., Dencheva, N., et al. 2026, JWST Calibration Pipeline, Space Telescope Science Institute, DOI 10.5281/zenodo.6984365

Castelli, F., & Kurucz, R. L. 2003, in *Modelling of Stellar Atmospheres,* ed. N. Piskunov, W. W. Weiss, & D. F. Gray, p A20

Cernicharo, J., Heras, A. M., Tielens, A. G. G. M., et al. 2001, ApJL, L123

Cerrigone, L., Hora, J. L., Umana, G., et al. 2011, ApJ, 738, 121

Cesarsky, D., Lequeux, J., Ryter, C., & Gérin, M. 2000, A&A, 354, L87

Chiar, J. E., Pendleton, Y. J., Geballe, T. R., & Tielens, A. G. G. M. 1998, ApJ, 507, 281

Chown, R., Sidhu, A., Peeters, E., et al. 2024, A&A, 685, A75

Clark, N., Peeters, E., Cami, J., et al. 2026, in preparation

Clark, N., Peeters, E., Cami, J., et al. in preparation

Das, D., Cami, J., Bhatt, C., et al. 2026, in preparation

de Graauw, T., Haser, L. N., Beintema, D. A., et al. 1996, A&A, 315, L49

Demyk, K., Joblin, C., de Bentzmann, L., et al. 2026, arXiv 2607.16018

De Smedt, K., Van Winckel, H., Karakas, A. I., et al. 2012, A&A, 541, A67

Draine, B. T. & Bertoldi, F. 1996, ApJ, 468, 269

Drossart, P., Fouchet, Th., Crovisier, J., et al. 1999, "The Universe as Seen by ISO," ed. P. Cox & M. F. Kessler, ESA SP-427, 169

Gaia Collaboration, Prusti, T., de Bruijne, J. H. J., et al. 2016, A&A, A595

Gaia Collavoration, Vallenari, A., Brown, A G. A., et al. 2023, A&A, 674, A1

Gardner, J. C., Mather, J. C., Abbott, R. et al. 2023, PASP, 135, 68001

Gasman, D., Argyriou, I., Law, D. R., et al. 2025, A&A, 697, A58

Geballe, T. R., Tielens, A. G. G. M., Kwok, S., & Hrivnak, B. J. 1992, ApJL, 387, L89

Geballe, T. R., & van der Veen, W. E. C. J. 1990, A&A, 235, L9

Gillett, F. C., Forrest, W. J., & Merrill, K. M. 1973, ApJ, 183, 87

Gillett, F. C., Kleinmann, D. E., Wright, E. L., & Capps, R. W. 1975, ApJL, 198, L65

Gordon, I. E., Rothman, L. S., Hargreaves, R. J., et al. 2026, JQSRT, 353, 109807

Gordon, K. D., & Law, D. R. 2026, ApJ, submitted

Gordon, K. D., Bohlin, R., Sloan, G. C., et al. 2022, AJ, 163, 267

Goto, M., Gaessler, W., Hayano, Y., et al. 2003, ApJ, 589, 419

Graczyk, D., Pietrzyński, G., Thompson, I. B., et al. 2020, ApJ, 904, 13

Groenewegen, M. A. T., & Sloan, G. C. 2018, A&A, 609, A114

Gruendl, R. A., Chu, Y.-H., Seale, J. P., et al. 2009, ApJL, 688, L9

Hron, J., Loidl, R., Höfner, S., et al. 1998, A&A, 335, L69

Hony, S., Waters, L. B. F. M., & Tielens, A. G. G. M. 2002, A&A, 390, 533

Houck, J. R., Roellig, T. L., van Cleve, J., et al. 2004, ApJS, 154, 18

Hrivnak, B. J., & Kwok, S. 1991, ApJ, 368, 564

Hrivnak, B. J., & Kwok, S., & Geballe, T. R. 1994, ApJ, 420, 783

Jakobsen, P., Ferruit, P., Alves de Oliveira, C., et al. 2022, A&A, 661, A80

Jensen, P. A., Shannon, M. J., Peeters, E., et al. 2022, A&A, 665, A13

Joblin, C., Tielens, A. G. G. M., Allamandola, L. J., & Geballe, T. R. 1996, ApJ, 458, 610

Jones, O. C., Álvarez-Márquez, J., Sloan, G. C., et al. 2023, MNRAS, 523, 2519

Kessler, M. F., Steinz, J. A., Anderegg, M. E., et al. 1996, A&A, 315, L27

Kraemer, K. E., Sloan, G. C., Bernard-Salas, J., et al. 2006, ApJL, 345, L25

Kwok, S., Volk, K. M., & Hrivnak, B. J. 1989, ApJL, 345, L15

Law, D. R., Argyriou, I., Gordon, K. D., et al. 2025, AJ, 169, 67

Leger, A., & Puget, J. L. 1984, A&A, 137, L5

Leisy, P., & Dennefeld, M. 2006, A&A, 456, 451

Lequeux, J., & Jourdain de Muizon, M. 1990, A&A, 240, L19

Leung, C. M. 1975, ApJ, 199, 340

Leung, C. M. 1976, JQRST, 16, 559

Li, J., García-Hernaández, D. A., Manchado, A., et al. 2026, ApJL, submitted

Mainzer A., Bauer J., Cutri R. M., et al. 2014, ApJ, 792, 30

Malek, S. E., Cami, J., & Bernard-Salas, J. 2012, ApJ, 744, 16
Mainzer A., Bauer J., Grav, T., et al. 2011, ApJ, 731, 53
Martin, P. G., & Rogers, C. 1987, ApJ, 322, 374
Matsuura, M., Bernard-Salas, J., Lloyd Evans, T., et al. 2014, MNRAS, 439, 1472
Misselt, K., Witt, A. N., Gordon, K. D., et al. 2025, A&A, 700, A158
Morgan, D. H., & Parker, Q. A. 2006, MNRAS, 296, 921
Ochsenbein, F., Bauer, P., & Marcout, J. 2000, A&AS, 143, 23
Olnon, F. M., Raimond, E., Neugebauer, G., et al. 1986, A&AS, 65, 607
Peeters, E., Allamandola, L. J., Bauschlicher, C. W., et al. 2004, ApJ, 604, 252
Peeters, E., Hony, S., Van Kerckhoven, C., et al. 2002, A&A, 390, 1089
Pietrzyński, G., Graczyk, D., Gallenne, A., et al. 2019, Nature, 567, 200
Pino, T., Dartois, E., Cao, A.-T., et al. 2008, A&A, 490, 665
Pontoppidan, K. M., Salyk, C., Banzatti, A., et al. 2024, ApJ, 963, 158
Pukītis 2026, ApJ, 1006, 104
Rauscher, B. J. 2024, PASP, 136 015001
Ricca, A., Sloan, G. C., Peeters, E., et al. 2026, in preparation
Ridgway, S. T., Carbon, D. F., & Hall, D. N. B. 1978, ApJ, 225, 138
Rieke, G. H., & Lebofsky, M. J. 1985, ApJ, 288, 618
Rouleau, F., & Martin, P. G. 1991, ApJ, 377, 526
Sandford, S. A., Allamandola, L. J., Tielens, A. G. G. M., et al. 1991, ApJ, 371, 607
Sandford, S. A., Bernstein, M. P., & Materese, C. K. 2013, ApJS, 205, 8
Sanduleak, N., MacConnell, D. J., & Phillip, Davis, A. G. D. 1978, PASP, 90, 621
Shaw, R. A., Stangehellini, L., villaver, E., & Mutschler, M. 2006, ApJS, 167, 201
Sloan, G. C., Aringer, B., Kraemer, K. E., et al. 2026, ApJ, 1002, 116
Sloan, G. C., Hayward, T. L., Allamandola, L. J., et al. 1999, ApJL, 513, L65
Sloan, G. C., Jura, M. Duley, W. W., et al. 2007, ApJ, 664, 1144
Sloan, G. C., Kraemer, K. E., McDonald, I., et al. 2016, ApJ, 826, 44
Sloan, G. C., Lagadec, E., Zijlstra, A. A., et al. 2014, ApJ, 791, 28
Snow, T. P., & Witt, A. N. 1995, Science, 270, 1455
Speck, A. K., Barlow, M. J., & Skinner, C. J. 1997, MNRAS, 288, 431
Sterling, N. C., Ibañez, C., Wahlgren, G., et al. 2026, BAAS, 58, 283.02
Szczerba, R., Hajduk, M., Pavlenko, Y. V., et al. 2020, A&A, 641, A142
Teplitz, H. I., Desai, V., Armus, L., et al. 2007, ApJ, 659, 941
van Aarle, E., van Winckel, H., Lloyd Evans, T., et al. 2011, A&A, 530, 90
van Loon, J. Th., Cohen, M., Oliveira, J. M., et al. 2008, A&A, 487, 1055
Volk, K., Hrivnak, B. J., Matsuura, M., et al. 2011, ApJ, 735, 127
Volk, K., Sloan, G. C., & Kraemer, K. E. 2020, Ap&SS, 365, 88
Wenger, M., Ochsenbein, F., Egret, D., et al. 2000, A&AS, 143, 9
Werner, M. W., Roellig, T. R., Low, F. J., et al. 2004, ApJS, 154, 1
Willner, S. P., Soifer, B. T., Russell, R. W., et al. 1977, ApJL, 217, L121
Wright, E. L., Eisenhardt, P. R. M., Mainzer, A. K., et al. 2010, AJ, 140, 1868
Wright, G. S., Rieke, G. H., Glass, A., et al. 2023, PASP, 135, 48003
Zaritsky, D., Harris, J., Thompson, I., & Grebel, E. K. 2004, AJ, 128, 1606